using CT images, and investigated the factors influencing compensatory hypertrophy after unilateral nephrectomy.

MATERIAL AND METHODS

Patient Population

From December 2003 to January 2008, a total of 202 patients underwent unilateral nephrectomy at Komaki City Hospital. Preoperative CT images were not available for 18 patients, and contrast media could not be administered to 12 patients because of low renal function or allergy to iodinated contrast medium. Furthermore, 30 patients underwent chemotherapy. These 60 patients were excluded from the present study. The remaining 142 patients, including 69 with renal cell carcinoma, 51 with urothelial carcinoma, 16 with an atrophic kidney, 5 kidney donors, and 1 with liposarcoma were enrolled. Of these patients, 104 were men and 38 were women. Their mean age was 62.8 ± 13.0 (mean ± SD) years (range 22-93). A total of 53 patients were receiving medications for hypertension and 10 for diabetes.

Imaging Procedures

The patients were injected with 74 MBq technetium-99m dimercaptosuccinic acid (DMSA). After 2 hours, posterior images were obtained using a Hitachi/Philips SKY Light gamma camera (Japan) equipped with a low-energy, general-purpose collimator. The regions of interest were drawn on the images for both kidneys showing the calculated percentage of split function. Of the 142 patients, 140 underwent preoperative DMSA renal scintigraphy.

Contrast-enhanced CT scans were obtained with a multislice 16-row unit (Sensation 16 Cardiac, Siemens, Germany) at a table speed of 20 mm/s and a slice thickness of 5 mm, with a 100-mL injection of intravenous iodinated contrast agent (flow 2 mL/s). The regions of interest were drawn around the kidneys, excluding the peripelvic fat and renal pelvis from the images by experienced radiologists who were unaware of the patients' clinical information. Functioning renal tissue was determined as the normally enhanced areas on the CT images, and tumors and cysts were excluded from the regions of interest. RPV was calculated using Volume software (Siemens, Germany), three-dimensional image reconstruction program. All patients underwent CT before unilateral nephrectomy. Also, 140 and 122 patients underwent CT at 1 week and 6 months postoperatively, respectively.

Serum creatinine was simultaneously determined, and the GFR was calculated using the revised modified diet in renal disease formula (GFR [mL/min/1.73 m^2] = 0.741 × 175 × $age^{-0.203}$ × $creatine^{-1.154}$ [× 0.742 for female sex]). The single GFR of the remaining kidney was calculated from the total GFR and the uptake ratio of the remaining kidney on DMSA renal scintigraphy.

Statistical Analysis

Continuous variables are presented as the mean ± SD and compared using Student's t test. One-way analysis of variance was used to test for an association between the percentage of DMSA uptake (%DMSA) in the resected kidney and the increase in contralateral RPV. The differences in the prevalence of hypertension and diabetes were evaluated using the χ^2 test. Multivariate stepwise regression analysis was used to test the relationship between the increased rate of remnant RPV and patient characteristics (sex, age, body surface area, %DMSA of resected kidney, preoperative GFR of remaining kidney, hypertension, and diabetes mellitus). Significant predictors of a GFR decrease were investigated using logistic regression analysis on the increased rate of the remnant RPV. All tests were 2-sided, and $P < .05$ was considered statistically significant. All statistical analyses were performed using Statistical Package for Social Sciences software (SPSS, Chicago, IL).

Table 1. Patient characteristics

Characteristic	Value
Patients (n)	142
Sex	
Male	104
Female	38
Age (y)	62.8 ± 13.0
Pathologic findings	
Renal cell carcinoma	69
Urothelial carcinoma	51
Atrophic kidney	16
Renal transplant donor	5
Liposarcoma	1
Serum creatinine (mg/dL)	
Preoperatively	0.87 ± 0.24
6 mo postoperatively	1.15 ± 0.28
GFR (mL/min/1.73 m^2)	
Preoperatively	66.0 ± 18.3
Remaining kidney	
Preoperative	40.3 ± 11.9
6 mo postoperatively	47.8 ± 15.5
RPV of remaining kidney (cm^3)	
Preoperatively	164.2 ± 37.9
Postoperatively	
1 wk	184.1 ± 44.7
6 mo	178.8 ± 41.1
Preoperative RPV of resected kidney (cm^3)	120.4 ± 55.2

GFR, glomerular filtration rate; RPV, renal parenchymal volume.

RESULTS

The patient data are summarized in Table 1. The %DMSA in the resected kidney was 37.2% ± 15.3%. The preoperative serum creatinine level was 0.87 ± 0.24 mg/dL (range 0.43-1.76) and increased to 1.11 ± 0.30 mg/dL (range 0.49-1.98) at 1 week postoperatively. The mean GFR of the remaining kidney increased by 27.1% from 40.3 to 49.8 mL/min/1.73 m^2 at 1 week after nephrectomy ($P < .001$).

The preoperative RPV of the remaining kidney was 164.2 ± 37.9 cm^3 and that of the resected kidney was 120.4 ± 55.2 cm^3. The RPV of the remaining kidney increased by 12.1% to 184.1 ± 44.7 cm^3 ($P < .001$) and by 8.9% to 178.8 ± 41.1 cm^3 at 1 week and 6 months after surgery, respectively ($P < .001$).

The patients were divided into 5 groups according to the %DMSA in the resected kidney. The increase in

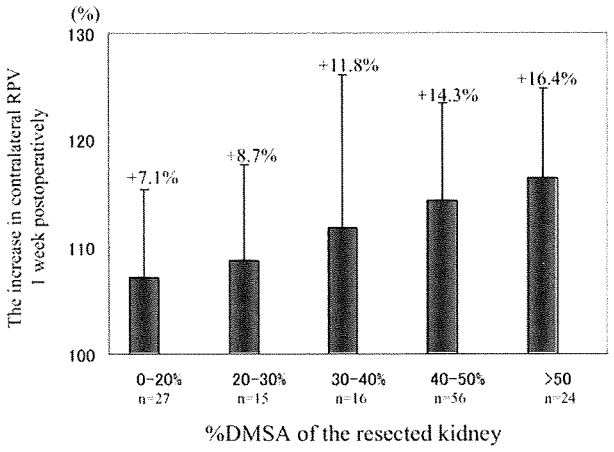

Figure 1. Correlation between preoperative percentage of technetium-99m dimercaptosuccinic acid uptake in resected kidney and contralateral renal parenchymal volume increase at 1 week postoperatively.

RPV was 7.1% in group 1 (%DMSA 0-20, n = 27), 8.7% in group 2 (%DMSA 20-30, n = 15), 11.8% in group 3 (%DMSA 30-40, n = 16), 14.3% in group 4 (%DMSA 40-50, n = 56), and 16.4% in group 5 (%DMSA >50, n = 24; Fig. 1). One-way analysis of variance detected statistically significant differences among the groups (P = .003).

Multivariate regression analysis revealed that the increase in RPV was positively associated with the %DMSA in the resected kidney (P < .001) and negatively associated with patient age (P = .008). Furthermore, no statistically significant association was noted for sex (P = .112), body surface area (P = .298), preoperative GFR of the remaining kidney (P = .452), or the presence of hypertension (P = .182) or diabetes mellitus (P = .060; Table 2).

For subanalysis, the study population was stratified into 2 groups according to the increase in RPV at 1 week to determine its relationship with renal function deterioration. Group 1 included patients with an RPV increase of <15% and group 2 those with an RPV increase of ≥15% (Table 3). The patients in group 1 were significantly older and had a lower %DMSA in the resected kidney compared with group 2 patients. At 6 months postoperatively, 37.2% (35/94) and 13.0% (6/46) of patients in groups 1 and 2, respectively, exhibited a >10% decrease in the estimated GFR compared with the corresponding values at 1 week postoperatively. Logistic regression analysis showed that the relative risk of decrease in renal function in group 1 patients was 4.1-fold (95% confidence interval 1.6-10.7; P = .004) greater than that in group 2 patients.

COMMENT

Unilateral nephrectomy in a patient with 2 normally functioning kidneys induces the immediate adaptation in both function and structure in the remaining kidney. Anderson et al.[4] reported that the effective renal plasma flow increased by 32.5% at 1 week, 30.1% at 1 year, and 37.2% at 10 years compared with the baseline preoperative values after donor nephrectomy. Indudhara et al.[10] evaluated renal transplant donors with fibromuscular dysplasia of the renal arteries and reported that the effective renal plasma flow in the remaining kidney had increased by 25% on postoperative day 5 and by 29% at 1 year postoperatively. With regard to the kidney volume, Mullerad et al.[11] evaluated renal hypertrophy after unilateral nephrectomy using DMSA renal scintigraphy. The mean age of their study population was 61.5 years, and the mean uptake ratio in the resected kidney was 40.74%. They reported that the RPV increased postoperatively by 11% ± 17.5%. Our patients' characteristics were almost identical to those of their patients, and the increase in RPV was 12.1% at 1 week and 8.9% at 6 months. Although the resected kidneys had lower function than the remaining kidneys, their average contribution to the overall baseline renal function was significant enough to cause a compensatory change in the remaining contralateral kidney.

Table 2. Correlation between patient characteristics and increase in RPV 1 week after nephrectomy

Factor	*P* Value
Sex	0.122
Age	.008
Body surface area	.298
%DMSA of resected kidney	<.001
Preoperative GFR of remaining kidney	.452
Hypertension	.182
Diabetes mellitus	.060

%DMSA, percentage of technetium-99m dimercaptosuccinic acid uptake; GFR, glomerular filtration rate.

Previously, we investigated the compensatory RPV increase of the normal side after nephron-sparing surgery.[12] In that study, we reported that the RPV of the normal kidney had increased by 9.6% at 1 week and 9.3% at 6 months after surgery. The contribution of the renal function in the operated side to the total renal function was 49.5%. In the present study, when the function of the resected kidney was 40%-50%, the RPV of the remaining kidney increased by 14.3% at 1 week after unilateral nephrectomy, a much greater increase than that after nephron-sparing surgery.

In our present study of unilateral nephrectomy and in our previous study of nephron-sparing surgery, we showed that the RPV increases and reaches a plateau within 1 week. It is unlikely that rapid histologic reconstruction is completed within a brief period of 1 week. Many studies have reported on the hemodynamic and structural changes after unilateral nephrectomy. The control of renal blood flow involves a complex interaction between circulating hormones and several vasoactive humoral factors in combination with the autonomic nervous system

Table 3. Patient characteristics stratified by increase in RPV 1 week postoperatively

Characteristic	RPV Increase		*P* Value
	<15% (Group 1)	≥15% (Group 2)	
Patients (n)	94	46	
Sex			.309
Male	71	31	
Female	23	15	
Age (y)	64.6 ± 12.0	58.7 ± 14.1	.012
Hypertension			.205
Yes	55	32	
No	39	14	
Diabetes mellitus			.369
Yes	86	44	
No	8	2	
%DMSA of resected side (%)	33.3 ± 15.6	44.7 ± 11.9	<.001
Serum creatinine level (mg/dL)			
Preoperatively	0.90 ± 0.26	0.81 ± 0.21	.042
Postoperatively			
1 wk	1.09 ± 0.31	1.16 ± 0.30	.161
6 mo	1.15 ± 0.28	1.13 ± 0.28	.643
GFR (mL/min/1.73 m^2)			
Preoperatively	64.1 ± 19.3	70.2 ± 15.8	.067
Remaining kidney	41.4 ± 12.2	38.6 ± 11.2	.201
1 wk	51.3 ± 14.4	47.0 ± 13.4	.089
6 mo	47.2 ± 12.6	49.5 ± 20.2	.438

Abbreviations as in Tables 1 and 2.

and the autoregulatory capacity of the kidney. It has been reported that the renal blood flow increases within 2 days of the reduction in renal vascular resistance in nephrectomized rats.[13,14] Histologic analysis revealed the primary site of hypertrophy is the cortex, in which proximal tubular cell hypertrophy, collecting tubular cell enlargement, and glomerular mesangial expansion occur within weeks after nephrectomy.[15,16] The hypertrophic response to unilateral nephrectomy seems to be secondary to renal hemodynamic changes. Renal blood flow is difficult to measure noninvasively and, to our knowledge, no report has assessed sequential hemodynamic changes after radical nephrectomy. The increase in RPV at 1 week observed in our study would be a result of an enlarged vascular bed caused by increased renal blood flow. Limited to a short period, it might be possible to estimate the renal blood flow by calculating the RPV.

We found that the change in contralateral RPV at 1 postoperative week was favorable for renal function until ≥6 postoperative months. Thus, renal functional deterioration can be predicted by measuring the RPV at 1 week postoperatively. We suspect that kidneys with a lesser increase in size after contralateral nephrectomy might have poorer compensatory potential and thus a greater risk of renal insufficiency. It is still not clear whether an increase in renal blood flow and hypertrophy will ultimately lead to renal insufficiency. Some have reported that unilateral nephrectomy might negatively affect the remaining kidney,[11,17,18] and others have reported no increased risk for the development of renal failure.[19] A larger sample size and longer follow-up might be required to detect long-term changes in RPV and renal function in various clinical conditions.

CONCLUSIONS

The change in contralateral RPV occurred during the first week after nephrectomy and remained stable for ≥6 months. The change in RPV increases when the removed kidney has greater function and decreases with age. Whether the renal function at 6 months will deteriorate can be predicted by measuring the RPV at 1 week postoperatively.

References

1. Johansson M, Moonen M. Prediction of post-operative glomerular filtration rate after nephrectomy for renal malignancy. *Clin Physiol.* 2001;21:688-692.
2. Tanaka N, Fujimoto K, Tani M, et al. Prediction of the postoperative renal function by the preoperative serum creatinine level and 3-dimensional diagnostic image reconstruction in patients with renal cell carcinoma. *Urology.* 2004;64:904-908.
3. Sorbellini M, Kattan MW, Snyder ME, et al. Prognostic nomogram for renal insufficiency after radical or partial nephrectomy. *J Urol.* 2006;176:472-476.
4. Anderson RG, Bueschen AJ, Lloyd LK, et al. Short-term and long-term changes in renal function after donor nephrectomy. *J Urol.* 1991;145:11-13.
5. Ito K, Nakashima J, Hanawa Y, et al. The prediction of renal function 6 years after unilateral nephrectomy using preoperative risk factors. *J Urol.* 2004;171:120-125.
6. Liu B, Preisig PA. Compensatory renal hypertrophy is mediated by a cell cycle-dependent mechanism. *Kidney Int.* 2002;62:1650-1658.
7. Kotre CJ, Owen JP. Method for the evaluation of renal parenchymal volume by X-ray computed tomography. *Med Biol Eng Comput.* 1994;32:338-341.
8. Nyengaard JR, Bendtsen TF. Glomerular number and size in relation to age, kidney weight, and body surface in normal man. *Anat Rec.* 1992;232:194-201.

9. Widjaja E, Oxytoby JW, Hale TL, et al. Ultrasound measured renal length versus low dose CT volume in predicting single kidney glomerular filtration rate. *Br J Radiol.* 2004;77: 759-764.
10. Indudhara R, Kenney PJ, Bueschen AJ, et al. Live donor nephrectomy in patients with fibromuscular dysplasia of the renal arteries. *J Urol.* 1999;162:678-681.
11. Mullerad M, Kastin A, Issaq E, et al. The value of quantitative 99m technetium dimercaptosuccinic acid renal scintigraphy for predicting postoperative renal insufficiency in patients undergoing nephrectomy. *J Urol.* 2003;169:24-27.
12. Funahashi Y, Hattori R, Yamamoto T, et al. Ischemic renal damage after nephron sparing surgery in patients with normal contralateral kidney. *Eur Urol.* In press.
13. Sigmon DH, Gonzalez-Feldman E, Cavasin MA, et al. Role of nitric oxide in the renal hemodynamic response to unilateral nephrectomy. *J Am Soc Nephrol.* 2004;15:1413-1420.
14. Valdivielso JM, Perez-Barriocanal F, Garcia-Estan J, et al. Role of nitric oxide in the early renal hemodynamic response after unilateral nephrectomy. *Am J Physiol.* 1999;276:R1718-R1723.
15. Lee GSL, Nast CC, Peng SC, et al. Differential response of glomerular epithelial and mesangial cells after subtotal nephrectomy. *Kidney Int.* 1998;53:1389-1398.
16. Preisig P. What makes cells grow larger and how do they do it? Renal hypertrophy revisited. *Exp Nephrol.* 1999;7:273-283.
17. Brenner BM, Meyer TW, Hostetter TH. Dietary protein intake and the progressive nature of kidney disease: the role of hemodynamically mediated glomerular injury in the pathogenesis of progressive glomerular sclerosis in ageing, renal ablation, and intrinsic renal disease. *N Engl J Med.* 1982;307:652-659.
18. Tapson JS. End-stage renal failure after donor nephrectomy. *Nephron.* 1986;42:262-264.
19. Ladefoged J. Renal failure 22 years after kidney donation. *Lancet.* 1992;339:124-125.

Direct Visualization of Renal Hemodynamics Affected by Carbon Dioxide–induced Pneumoperitoneum

Naoto Sassa, Ryohei Hattori, Tokunori Yamamoto, Masashi Kato, Tomonori Komatsu, Yoshihisa Matsukawa, Yasuhito Funahashi, and Momokazu Gotoh

OBJECTIVES To examine the direct renal hemodynamics during carbon dioxide pneumoperitoneum in both human and porcine models. Laparoscopic living donor nephrectomy has become widespread because of its minimally invasive nature. However, it has been clear that the renal hemodynamics and function are affected during carbon dioxide pneumoperitoneum.

METHODS The erythrocyte velocity in the cortical peritubular capillary (CPC) was monitored and measured during laparoscopic nephrectomy on human donors and laparoscopic partial nephrectomy on humans with renal cell carcinoma during carbon dioxide pneumoperitoneum (pressure of 8, 12, 15, 18, and 20 mm Hg). We used a direct imaging system of renal microcirculation by magnifying endoscopy, as previously described. We maintained the same pressure for 5 minutes. In the porcine model (6 pigs), we measured the erythrocyte velocity in the CPC using the same method during carbon dioxide pneumoperitoneum (pressure of 0, 5, 10, 15, 20, and 25 mm Hg).

RESULTS The erythrocyte velocity in the renal artery did not change during increased carbon dioxide pneumoperitoneum. When the pneumoperitoneal pressure was 25 mm Hg, we found that >90% of the erythrocyte velocity in the CPC was nonflowing. In the human model, the erythrocyte velocity in the CPC decreased when the carbon dioxide pneumoperitoneum pressure was 12 mm Hg.

CONCLUSIONS The erythrocyte velocity in the CPC decreased during carbon dioxide pneumoperitoneum in all kidneys in both the human and the porcine models. However, erythrocyte velocity in the renal artery did not change during carbon dioxide pneumoperitoneum. After stopping the pneumoperitoneum, the erythrocyte velocity in the CPC recovered immediately. The findings of our study have shown that the suitable carbon dioxide pneumoperitoneal pressure for renal microcirculation is <8 mm Hg for laparoscopic surgery. UROLOGY 73: 311–315, 2009. © 2009 Published by Elsevier Inc.

Laparoscopic surgery has been indicated for an increasing number of patients in many fields because of its minimally invasive nature. However, carbon dioxide-induced pneumoperitoneum is essential for laparoscopic surgery, and its complications include pulmonary embolism, venous circulatory disorder, and subcutaneous emphysema. Also, the pneumoperitoneal pressure leads to a decrease in the urine volume during surgery, but it seems to not have affected kidney function according to some reports.[1-5] Nguyen et al.[6] compared laparoscopic surgery with open surgery for gastric bypass and reported on the relationship between the intraoperative urine volume and kidney function. At 1 hour after starting laparoscopic surgery, the urine volume in the laparoscopic surgery group was 64% lower than that in the open surgery group. The postoperative urine volume was also 31%-50% lower. However, no published studies have reported on the reason this phenomenon occurs. Previously, Hattori et al.[7] reported on the correlation between the peritubular flow velocity in the transplanted kidney in the nonheart-beating donor and subsequent graft function using an extended endoscope. They initially examined whether the renal microcirculation was influenced by the pneumoperitoneal pressure under direct vision using the same endoscope.

MATERIAL AND METHODS

Animal Model

We used 6 six-month-old female pigs (left kidney). Under general anesthesia with ketamine hydrochloride, surgery was performed. For intraoperative management under anesthesia, the electrocardiogram, central venous pressure (CVP), urine

From the Department of Urology, Nagoya University Graduate School of Medicine, Nagoya, Aichi, Japan

Reprint requests: Naoto Sassa, M.D., Department of Urology, Nagoya University Graduate School of Medicine, 65 Tsurumai-chyo, Shyowa-ku, Nagoya, Aichi 455-8550 Japan. E-mail: sassa@med.nagoya-u.ac.jp

Submitted: April 18, 2008, accepted (with revisions): September 22, 2008

0090-4295/09/$34.00
doi:10.1016/j.urology.2008.09.047

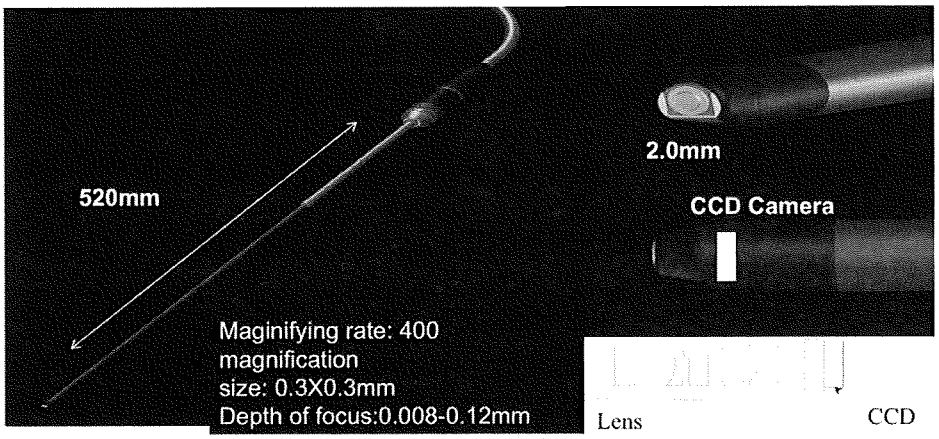

Figure 1. Measuring device. Renal cortical peritubular capillaries (CPCs) visualized with laparoscopic probe, a charge-coupled device video microscope with tip diameter of 2 mm and length of 520 mm. Probe magnifying rate 400×, size 0.3 × 0.3 mm, depth of focus 0.008-0.012 mm, permitting identification of individual erythrocytes.

volume, and transfusion rate were monitored. During surgery, a drip solution was intravenously injected, and the transfusion rate was established as 40 mL/h to standardize the anesthesia conditions in this study. Intraoperatively, the pigs were placed in the right-sided position. The adipose tissue around the kidney was exfoliated using a transabdominal approach to expose the renal parenchymal surface. The pneumoperitoneal pressure was elevated in a step-wise manner (5, 10, 15, 20, and 25 mm Hg), and each pressure was maintained for 5 minutes to measure the peritubular capillary erythrocyte rate (cortical peritubular capillary [CPC]). Simultaneously, the renal arterial trunk blood flow was determined using an electromagnetic flow meter under the same pressure. Next, open surgery was performed, and the CPC and renal arterial blood flow were measured in the absence of pneumoperitoneal pressure as control values. In each pig, microcirculation was determined at multiple points.

Also, we performed renal biopsy with the needle biopsy gun (16-gauge) at that time before starting the pneumoperitoneum and maintained the pressure at 20 mm Hg for 2 hours after starting laparoscopic surgery to determine the histopathologic changes. The histopathologic stain used was periodic acid-Schiff. Changes were assessed by 1 pathologist with microscopy (magnification ×200).

Clinical Cases

Two patients were included in the study; 1 underwent laparoscopic donor left nephrectomy (31-year-old woman with normal kidney function) and 1 underwent partial laparoscopic resection of the left kidney (48-year-old man with normal kidney function). Before surgery, both patients provided informed consent regarding the surgery and examination. For intraoperative management under anesthesia, the arterial pressure, electrocardiogram, CVP, urine volume, and transfusion rate were monitored. During surgery, the patients were placed in the right lateral decubitus position. Under systemic/epidural anesthesia, laparoscopic surgery was performed using the transperitoneal approach. After the renal capsule was exposed, the microcirculation was measured. During measurement, the pneumoperitoneal pressure was elevated in a step wise manner (8, 12, 15, and 18 mm Hg). Each pressure was maintained for 5 minutes to ensure no changes occurred in the vital signs, and the CPC was determined. In each patient, the measurement was performed at multiple points in the same kidney.

CPC Measurement

The renal CPC were visualized with a pencil-lens probe, charge-coupled device video microscope with a tip diameter of 1 mm, as previously studied. In the present study, we improved this probe to facilitate its use as a laparoscope. We developed a fine needle type (needle diameter 2 mm) to magnify renal endoscopy for laparoscopic surgery. The probe of the endoscopy had a magnification of 400× and depth of focus of 0.008-0.12 mm, permitting identification of individual erythrocytes (Fig. 1). The video signals were digitized with an analog-to-digital converter and fed into a digital videocassette recorder (DVCam, Sony, Tokyo, Japan) interfaced with a computer. The analysis was performed using the National Institutes of Health Image program combined with Matlab or specifically written programs. The peritubular capillary blood flow was recorded with the microscope brought into direct contact with the decapsulated renal surface through the port during laparoscopic surgery. The images were recorded on digital videocassette tapes before and after inducing the pneumoperitoneum. The consecutive images of blood flow were collected at a rate of 30 frames/s (size 0.3 × 0.3 mm). The images were analyzed using the freeze-frame mode. The velocity of the red blood cells in individual segments of the peritubular capillaries was analyzed using a specifically designed adaptation of a previously developed algorithm.[8] Specifically, a line segment was set along a capillary bed in sequentially videotaped images, and a spatiotemporal image was constructed (the line-shift method), allowing us to discern differences in the gray level during passage of red blood cells. The angle of a line-shift striped pattern was estimated to compute the erythrocyte velocity vector.

Renal arterial blood flow was measured using an electromagnetic flow meter. After the renal artery was exposed, electrodes were placed in this artery for measurement. The velocity was recorded with respect to the pneumoperitoneal pressure or serially.

Statistical Analysis

We analyzed the erythrocyte velocity of the CPC between each increase in pneumoperitoneal pressure using Wilcoxon's test. $P \leq .05$ was considered significant.

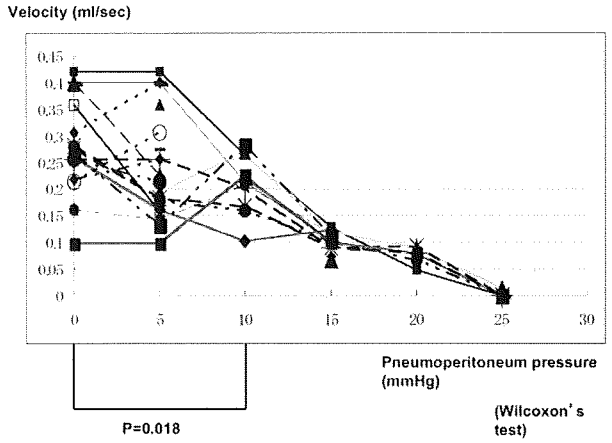

Figure 2. Erythrocyte velocity in cortical peritubular capillary (CPC) in animal model. Pneumoperitoneal pressure-related changes in CPC shown. CPC decreased with increase in pressure. Significant differences found between 0 mm Hg (open surgery) and 10 mm Hg ($P < .05$), as well as between 10 and 15 mm Hg ($P < .01$). When pneumoperitoneal pressure reached 25 mm Hg, most erythrocytes remained stationary.

RESULTS

Animal Model

The pneumoperitoneal pressure-related changes in the CPC are shown in Figure 2. The CPC decreased with an increase in this pressure. Significant differences were found between a pressure of 0 mm Hg (open surgery) and 10 mm Hg ($P < .05$), as well as between 10 and 15 mm Hg ($P < .01$). When the pneumoperitoneal pressure reached 25 mm Hg, most erythrocytes remained stationary. At this point, no marked changes had occurred in the vital signs (ie, arterial pressure, CVP, or heart rate). When the pneumoperitoneal pressure was reduced to 10 mm Hg, the CPC improved rapidly.

No pneumoperitoneal pressure elevation-related changes occurred in the renal arterial flow velocity (Fig. 3; $P > .05$).

Clinical Cases

As demonstrated in our animal model, the CPC decreased with an increase in the pneumoperitoneal pressure (Fig. 4). During measurement, no marked changes occurred in the vital signs (ie, arterial pressure, CVP, or heart rate). A highly significant difference was found in the CPC between 8 and 12 mm Hg ($P < .01$). When the pneumoperitoneal pressure was reduced to the initial value, the CPC improved rapidly.

Histopathologic Findings in Porcine Model

At 2 hours after starting laparoscopic surgery (we maintained the pneumoperitoneal pressure at 20 mm Hg), the histopathologic findings showed damage of the subcapsular renal cortex from the pneumoperitoneal pressure, including tubular vacuolation, cell detachment, and tubular damage. However, the glomerulus was not damaged by the pneumoperitoneal pressure (Fig. 5).

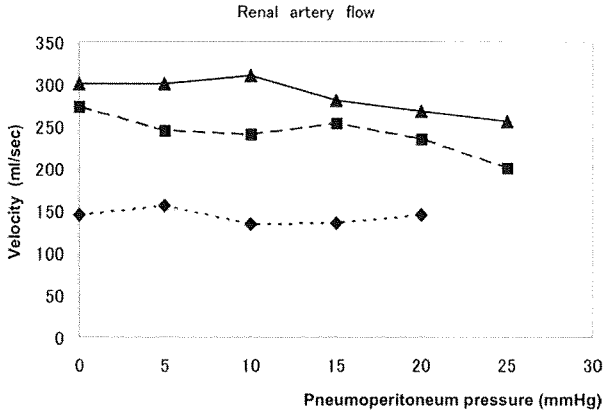

Figure 3. Erythrocyte velocity in renal artery in animal model. No pneumoperitoneal pressure elevation-related changes seen in renal arterial flow velocity ($P > .05$).

COMMENT

Pneumoperitoneal pressure leads to a decrease in the urine volume during surgery, but this may not affect kidney function. Nguyen et al.[6] compared laparoscopic surgery with open surgery for gastric bypass and reported on the relationship between the intraoperative urine volume and kidney function. At 1 hour after starting laparoscopic surgery, the urine volume in the laparoscopic surgery group was 64% lower than that in the open surgery group. The postoperative urine volume was also 31%-50% lower. After laparoscopic donor nephrectomy, initial urination after reperfusion is often delayed. McDougall et al.[9] indicated that an increase in the pneumoperitoneal pressure depended on the grade of oliguria. Hassan et al.[10] reported that oliguria occurred at a pneumoperitoneal pressure of 15 mm Hg, and that anuria developed at a pneumoperitoneal pressure of 30 mm Hg. In an animal experiment, the influence of intravascular catheter insertion on major blood vessels such as the renal artery or vein was investigated. No influence from the pneumoperitoneal pressure on the renal artery/vein was found. Also, our electromagnetic flow meter-based data did not confirm the influence of pneumoperitoneal pressure on the renal artery.

Chiu et al.[11] reported that the blood flow decreased by 60% at a pneumoperitoneal pressure of 15 mm Hg in a laser Doppler examination. In our animal model, significant differences were found in the CPC between pneumoperitoneal pressures of 0 mm Hg (open surgery) and 10 mm Hg ($P < .05$), as well as between 10 and 15 mm Hg ($P < .01$). At 25 mm Hg, most erythrocytes remained stationary. In our series, a significant difference was seen in the rate of decrease in the CPC between pneumoperitoneal pressures of 8 and 12 mm Hg during laparoscopic surgery ($P < .01$). Thus, the pneumoperitoneal pressure should be controlled to <8 mm Hg to eliminate its influence on renal microcirculation. We examined the peritubular capillaries and erythrocytes under direct vision, and initially reported the influence of pneumoperi-

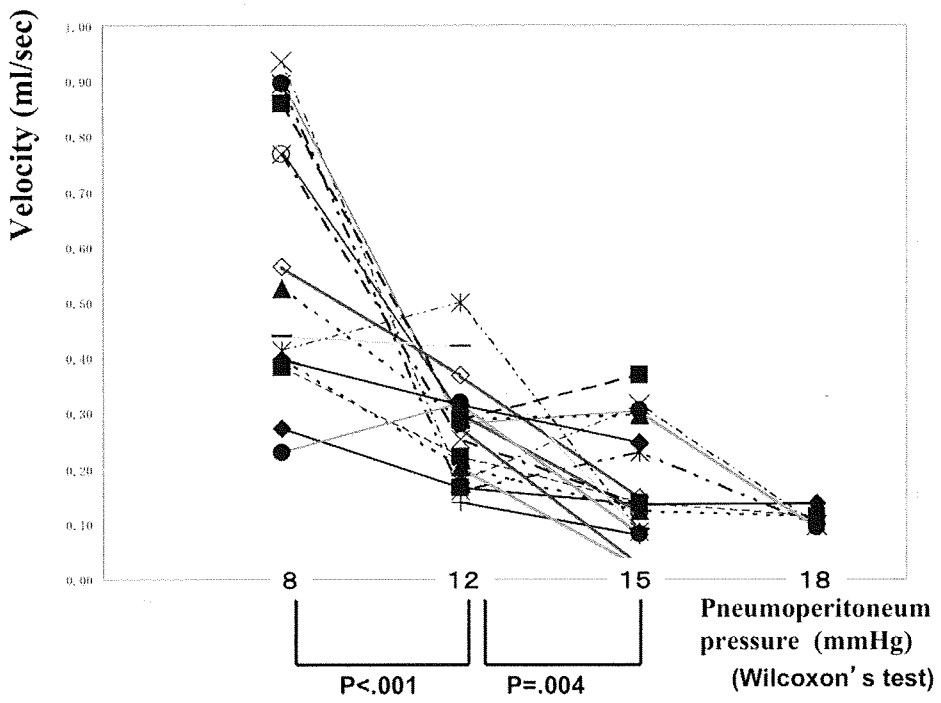

Figure 4. Erythrocyte velocity in cortical peritubular capillary (CPC) in clinical cases. As demonstrated in our animal model, CPCs decreased with increase in pneumoperitoneal pressure. A highly significant difference seen in CPCs between 8 and 12 mm Hg ($P < .01$). When pneumoperitoneal pressure was reduced to initial value, CPCs improved rapidly.

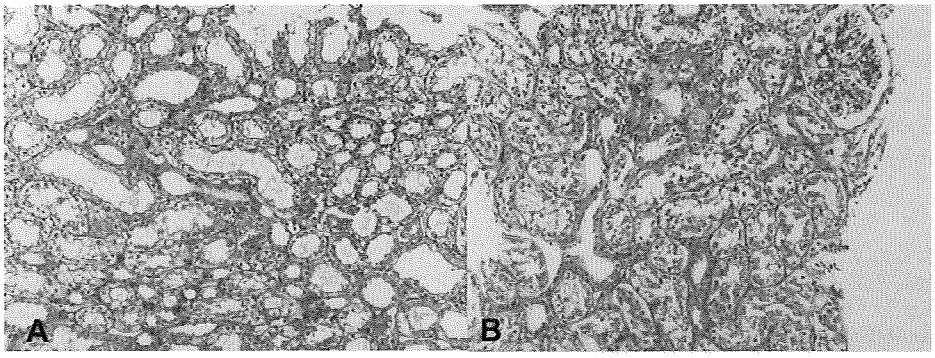

Figure 5. Histopathologic changes shown by microscopy with periodic acid-Schiff staining. Original magnification ×200. **(A)** We performed renal biopsy with the needle biopsy gun (16 gauge) at that time before inducing pneumoperitoneum. **(B)** Two hours after starting laparoscopic surgery, histopathologic findings showed damage from pneumoperitoneal pressure, including tubular vacuolation, cell detachment, and tubular damage; however, glomerulus was not damaged by pneumoperitoneal pressure.

toneal pressure on peritubular capillary blood flow, as well as an appropriate pneumoperitoneal pressure at which renal microcirculation was not affected.

Kron et al.[12] and Harman et al.[13] speculated that direct compression of the renal cortex or blood vessels might be involved in the mechanism by which an increase in pneumoperitoneal pressure decreases the urine volume. In rats, the peritubular capillary pressure is considered approximately 15 mm Hg. When the pneumoperitoneal pressure increases to ≥15 mm Hg, complete occlusion of the peritubular capillaries can occur, affecting tubular blood flow. We have confirmed that the peritubular capillary blood flow disturbance occurs even at a low pneumoperitoneal pressure, even when complete occlusion is absent. Shimizu et al.[14,15] reported on 0-hour biopsy specimens collected during laparoscopic donor nephrectomy. Histologic changes in the subcapsular renal cortex, including tubular necrosis and interstitial hemorrhage, were observed in 37.7% of patients who underwent retro-laparoscopic donor nephrectomy (pneumoperitoneal pressure 7 mm Hg) and in 46.7% of those who underwent laparoscopic donor nephrectomy with a transperitoneal approach (pneumoperitoneal pressure 10-15 mm Hg). However, no such changes were seen in any of the patients undergoing open surgery.

In our histopathologic study, we found tubular damage of the subcapsular renal cortex from the pneumoperito-

neal pressure, including tubular vacuolation, cell detachment, and tubular damage at 2 hours after starting laparoscopic surgery (pneumoperitoneal pressure maintained at 20 mm Hg). However, the glomerulus was not damaged by the pressure. This finding showed that only tubules were affected by the pneumoperitoneal pressure.

Furthermore, Kron et al.[12] reported that an increase in pneumoperitoneal pressure (≥25 mm Hg) led to acute renal dysfunction and that decompression rapidly relieved such dysfunction. Our data also showed that the discontinuation of the pneumoperitoneum rapidly elevated the CPCs in our series and in our animal model.

In investigating the influence of the pneumoperitoneal pressure on kidney function, the duration of surgery should be considered. We established the duration of the pneumoperitoneum at 5 minutes and investigated the phenomenon in humans. Neither measurement nor analysis has been previously accomplished. Wakizaka et al.[16] reported on the influence of the pneumoperitoneal pressure and the duration of surgery on a decrease in urine volume. In the future, this issue should also be examined further.

CONCLUSIONS

Many studies have concluded that oliguria is noted during surgery but with no marked differences in postoperative kidney function. However, histologic changes have been reported even at a low pneumoperitoneal pressure, suggesting kidney damage. We clarified the mechanism by examination under direct vision. The pneumoperitoneal pressure should be controlled to <8 mm Hg to maintain renal microcirculation.

References

1. Richards WO, Scovill W, Shin B, et al. Acute renal failure associated with increased intra-abdominal pressure. *Ann Surg.* 1983; 197:183-187.
2. Kirsch AJ, Kayton ML, Hensle TW, et al. Renal effects of CO_2 insufflation: oliguria and acute renal dysfunction in a rat pneumoperitoneum model. *Urology.* 1994;43:453-459.
3. Troppmann C, Pierce JL, Wiesmann KM, et al. Early and late recipient graft function and donor outcome after laparoscopic vs open adult live donor nephrectomy for pediatric renal transplantation. *Arch Surg.* 2002;137:908-916.
4. Rondon ET, Ho HS, Neuhaus AMC, et al. Effect of intravascular volume expansion on renal function during prolonged CO_2 pneumoperitoneum. *Ann Surg.* 2000;231:195-201.
5. Junghans T, Bohm B, Grundel K, et al. Does pneumoperitoneum with different gases, body positions, and intraperitoneal pressures influence renal and hepatic blood flow? *Surgery.* 1997;121: 206-211.
6. Nguyen NT, Perez RV, Fleming N, et al. Effect of prolonged pneumoperitoneum on intraoperative urine output during laparoscopic bypass. *J Am Coll Surg.* 2002;195:476-482.
7. Hattori R, Yoshinari O, Yamamoto T, et al. Direct visualization of cortical peritubular capillary of transplanted human kidney with reperfusion injury using a magnifying endoscopy. *Transplantation.* 2005;79:1190-1194.
8. Ogasawara Y, Takehara K, Yamamoto T, et al. Quantitative blood velocity mapping in glomerular capillaries by in vivo observation with an intravital video microscope. *Methods Inf Med.* 2000;39:175-178.
9. McDougall EM, Monk TG, Stuart J, et al. The effect of prolonged pneumoperitoneum on renal function in an animal model. *J Am Coll Surg.* 1996;182:317-328.
10. Hassan A, Razvi D, Vargas JC, et al. Oliguria during laparoscopic surgery: evidence for direct renal parenchymal compression as an etiologic factor. *J Endourol.* 1996;10:1-4.
11. Chiu AW, Chang LS, Birkett DH, et al. The impact of pneumoperitoneum, pneumoretroperitoneum, and gasless laparoscopy on the systemic and renal hemodynamics. *J Am Coll Surg.* 1995;181: 397-406.
12. Kron IL, Harman PK, Nolan SP, et al. The measurement of intra abdominal pressure as a criterion for abdominal re-exploration. *Ann Surg.* 1984;199:28-30.
13. Harman PK, Kron IL, McLachlan HD, et al. Elevated intraabdominal pressure and renal function. *Ann Surg.* 1984;196:594-597.
14. Shimizu T, Tanabe K, Miyamoto N, et al. Early and late histopathological changes in renal allograft procured by laparoscopic donor nephrectomy. *Clin Transplant.* 2006;20:11-15.
15. Shimizu T, Tanabe K, Ishida H, et al. Histopathological evaluation of 0-hr biopsy specimens of donor kidney procured by laparoscopic donor nephrectomy. *Clin Transplant.* 2004;18:24-28.
16. Wakizaka Y, Sano S, Koike Y, et al. Changes of arterial CO_2 and urine output by carbon dioxide insufflation of the peritoneal cavity during laparoscopic cholecystectomy. *Nippon Geka Gakkai Zasshi.* 1994;95:336-342.

EXPERIMENTAL CELL RESEARCH 315 (2009) 3052–3063

available at www.sciencedirect.com

ScienceDirect

www.elsevier.com/locate/yexcr

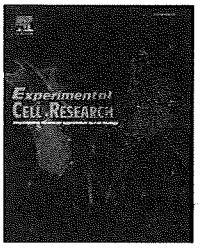

Research Article

Dynamic clustering and dispersion of lipid rafts contribute to fusion competence of myogenic cells

Atsushi Mukai[a], *Tomohiro Kurisaki*[b], *Satoshi B. Sato*[c], *Toshihide Kobayashi*[d], *Gen Kondoh*[e], *Naohiro Hashimoto*[a,*]

[a]*Department of Regenerative Medicine, National Institute for Longevity Sciences, National Center for Geriatrics and Gerontology, 36-3 Gengo, Morioka, Oobu, Aichi 474-8522, Japan*

[b]*Department of Growth Regulation, Institute for Frontier Medical Sciences, Kyoto University, 53 Shogoin-Kawahara-cho, Sakyo-ku, Kyoto 606-8507, Japan*

[c]*Research Center for Low Temperature and Material Sciences, Kyoto University, Yoshida-honmachi, Kyoto 606-8501, Japan*

[d]*Lipid Biology Laboratory, Discovery Research Institute, RIKEN, Wako, Saitama 351-0198, Japan*

[e]*Laboratory of Animal Experiments for Regeneration, Institute for Frontier Medical Sciences, Kyoto University, 53 Shogoin-Kawahara-cho, Sakyo-ku, Kyoto 606-8507, Japan*

ARTICLE INFORMATION

Article Chronology:
Received 31 March 2009
Revised version received 22 June 2009
Accepted 8 July 2009
Available online 14 July 2009

Keywords:
Myogenesis
Cell fusion
Lipid raft
M-cadherin
Myoblast
Membrane cholesterol

ABSTRACT

Recent research indicates that the leading edge of lamellipodia of myogenic cells (myoblasts and myotubes) contains presumptive fusion sites, yet the mechanisms that render the plasma membrane fusion-competent remain largely unknown. Here we show that dynamic clustering and dispersion of lipid rafts contribute to both cell adhesion and plasma membrane union during myogenic cell fusion. Adhesion-complex proteins including M-cadherin, β-catenin, and p120-catenin accumulated at the leading edge of lamellipodia, which contains the presumptive fusion sites of the plasma membrane, in a lipid raft-dependent fashion prior to cell contact. In addition, disruption of lipid rafts by cholesterol depletion directly prevented the membrane union of myogenic cell fusion. Time-lapse recording showed that lipid rafts were laterally dispersed from the center of the lamellipodia prior to membrane fusion. Adhesion proteins that had accumulated at lipid rafts were also removed from the presumptive fusion sites when lipid rafts were laterally dispersed. The resultant lipid raft- and adhesion complex-free area at the leading edge fused with the opposing plasma membrane. These results demonstrate a key role for dynamic clustering/dispersion of lipid rafts in establishing fusion-competent sites of the myogenic cell membrane, providing a novel mechanistic insight into the regulation of myogenic cell fusion.

Introduction

Skeletal muscle fibers are multinucleated cells that are derived from multinucleated myotubes. This muscle-specific syncytium is formed by the fusion of mononucleated myogenic progenitor cells (myoblasts) that are descendants of muscle stem cells called muscle satellite cells. Myoblasts show unique capacities, including multipotentiality [1] and the ability to fuse with each other or to existing myofibers in a cell-autonomous way during both postnatal growth and repair of skeletal muscle. Myoblast fusion consists of a

* *Corresponding author.*
E-mail address: nao@nils.go.jp (N. Hashimoto).

Abbreviations: CTB, cholera toxin B subunit; fPEG-Chol, fluorescein-labeled poly(ethylene glycol) cholesteryl ester; MCD, methyl-β-cyclodextrin

0014-4827/$ – see front matter © 2009 Elsevier Inc. All rights reserved.
doi:10.1016/j.yexcr.2009.07.010

series of steps: myoblast–myoblast contact, recognition, adhesion, and plasma membrane breakdown/union [2–4]. Each step of myoblast fusion is strictly regulated at cellular and subcellular levels. Plasma membrane breakdown/union is initially induced in a discrete area of the plasma membrane [5,6]. Thus, these studies imply specialization of presumptive fusion sites in the plasma membrane of myogenic cells.

The molecular mechanisms that control each step of myogenic cell fusion remain to be resolved, although a number of molecules have been implicated in regulating muscle fiber formation. Extracellular matrix receptor integrins and adhesion molecules such as cadherins, NCAM, CD9, CD81, and ADAMs may contribute to the regulation of the recognition/adhesion steps of myoblast fusion [7–9]. However, how they coordinate their functions in the recognition/adhesion steps at the discrete, presumptively fusion-competent site of the plasma membrane remains to be determined. In addition, it remains puzzling what molecular events trigger plasma membrane breakdown/union at the presumptively fusion-competent site after establishing the cell adhesion that is prerequisite for plasma membrane union.

Cholesterol is involved in maintaining membrane fluidity and the structure of lipid microdomains/rafts. The concentration of membrane cholesterol in myoblasts decreases prior to membrane fusion because an increase of membrane fluidity is required for plasma membrane union [10]. In fact, membrane fusion takes place within the cholesterol-free sites of the myoblast plasma membrane [11]. Furthermore, preventing membrane cholesterol levels from declining inhibits myoblast fusion [12]. Therefore, while cholesterol has been implicated in membrane fusion of myoblasts [12,13], the molecular mechanisms that regulate redistribution of membrane cholesterol at the presumptively fusion-competent sites of the plasma membrane remain to be identified.

Our previous study showed that the leading edge of lamellipodia of myogenic cells contain a fusion-competent site of plasma membrane [5]. To identify the key molecules that render the plasma membrane of lamellipodia fusion-competent, we determined a stimulus that enhances muscle cell fusion in vitro. We found that cholera toxin B subunit (CTB), which binds to ganglioside GM1 localized in lipid rafts/microdomains, enhanced muscle cell fusion. Furthermore, our data suggest a pivotal role for lipid rafts in both accumulation of adhesion molecules and redistribution of membrane cholesterol at the presumptively fusion-competent sites of the myoblast plasma membrane. The present study indicates that the dynamic clustering and dispersion of lipid rafts contributes to the control of myogenic cell fusion in a novel mode of action.

Materials and methods

Cell culture

The mouse myogenic cell clone Ric10 was established from muscle satellite cells of the normal gastrocnemius muscle of an adult female ICR mouse [1,5]. Ric10 cells were plated on dishes coated with type I collagen (Sumilon, Tokyo, Japan) and cultured at 37 °C under 10% CO_2 in pmGM consisting of Dulbecco's modified Eagle's medium supplemented with 20% fetal bovine serum (FBS), 2% Ultroser G (Biosepra, Cedex-Saint-Christophe, France), and glucose (4.5 mg/ml) [1,14–16]. For induction of myogenic differentiation, the cells were plated and cultured for 24 h in pmGM, and then the medium was changed to pmDM consisting of the chemically defined medium TIS [17,18] supplemented with 2% FBS.

For induction of myosheet formation, Ric10 cells were cultured in pmDM supplemented with 24 μM forskolin (Sigma, St. Louis, MO) or 125 ng/ml CTB (Calbiochem, San Diego, CA).

For removal of cholesterol from the plasma membrane, the cells were cultured in pmDM supplemented with 5 mM methyl-β-cyclodextrin (MCD) (Sigma). To quench an ability of MCD to remove membrane cholesterol, 0.625 mM cholesterol was preloaded on 5 mM MCD as described [19].

For micromass culture, the dissociated single cells were cultured in pmGM at a high density of 1×10^5 cells per 100-μl spot in a 35-mm dish. After incubation for at least 2 h, 1.5 ml of pmGM was carefully added to each dish.

Transfection to establish cell clone expressing GFP-GPI

pMiw-bsr, which was derived from pMiwCAT (kindly provided by H. Kondoh, Osaka University), contains a blasticidin-resistant gene (*bsr*) under the control of a β-actin promoter and a Rous sarcoma virus enhancer. Ric10 cells (2×10^4 cells in a 35-mm dish) were transfected with 0.9 μg of pCAAG-GFP-GPI [20,21] and 0.1 μg of pMiw-bsr in the presence of 4.5 μl of FuGENE6 transfection reagent (Roche Diagnostic, Mannheim, Germany) as described [17,18,22]. Ric10-derived clones constitutively expressing GFP-GPI were selected in the presence of blasticidin S (8 μg/ml) (Funakoshi, Tokyo, Japan). One of the isolated clones, designated GSS25, was used for further analyses because it preserved robust potential for myogenic differentiation and a high level of GFP-GPI expression.

Immunofluorescence and immunocytochemical analyses

Cells were grown on collagen-coated culture dishes, then fixed, permeabilized, and processed for immunostaining as described [1,5]. Primary antibodies included mouse monoclonal antibodies to sarcomeric myosine heavy chain (MyHC) (MF20; undiluted culture supernatant) [23], M-cadherin (1: 250 dilution; BD Biosciences, San Jose, CA), β-catenin (1:500 dilution; BD), p120-catenin (1:1000 dilution; BD), N-cadherin (1:100 dilution;BD), a rabbit polyclonal antibody to GFP (1:500 dilution, Medical Biological Laboratory, Nagoya, Japan), or a goat polyclonal antibody to PKA type II subunit (1:100 dilution; Upstate, Lake Placid, NY). Secondary antibodies included biotinylated antibodies to mouse (1:1000 dilution; Jackson ImmunoResearch Laboratory, Bar Harbor, ME) or goat (1:1000 dilution; Zymed Laboratories, San Francisco, CA) immunoglobulin G, Cy3-labeled antibodies to mouse immunoglobulin G (1:1000 dilution; Jackson ImmunoReseach Laboratory) and fluorescein isothiocyanate-labeled antibodies to rabbit immunoglobulin G (1:100 dilution; Cappel Laboratories, Downington, PA). The biotinylated antibodies were detected with Alexa 488 (Molecular Probes, Eugene, OR) or horseradish peroxidase-conjugated streptavidin. The peroxidase reaction was performed with 3,3-diaminobenzidine (Sigma). Cell nuclei were stained with 2, 4-diamidino-2-phenylindole dihydrochloride *n*-hydrate (DAPI) (0.5 μg ml^{-1}, Sigma) or Mayer's hematoxylin (Wako Pure Chemicals, Osaka, Japan). Samples were visualized using an inverted microscope (model IX71; Olympus, Tokyo, Japan) and a CCD camera (DP70; Olympus). Images were post-processed using Adobe Photoshop (Adobe Systems, San Jose, CA).

Visualization of localized F-actin, GM1, and cholesterol

F-actin in cells fixed with 4% paraformaldehyde was detected by incubation of the cells for 30 min in a solution containing Alexa Fluor 546-labelled phalloidin (66 nM) (Invitrogen, San Diego, CA). For detection of GM1, cells were placed on ice and incubated for 5 min with Alexa Fluor 488-labelled CTB (1 μM) (Molecular Probes, Eugene, OR). Then the cells were fixed with 4% paraformaldehyde. To visualize the distribution of cholesterol, cells were incubated for 5 min with fluorescein-labeled poly(ethylene glycol) cholesteryl ester (fPEG-Chol) (1 μM) [24,25], and then fixed with 4% paraformaldehyde.

Immunoblotting

Sample preparation and immunoblot analysis were performed as described [18,22,26]. Immune complexes were detected by colorimetry with a BCIP/NBT detection kit (Nacalai, Kyoto, Japan).

Time-lapse recording

Cells were cultured in neutral red-depleted pmDM and placed in a humid chamber (Tokai Hit, Fujinomiya, Japan) maintained at 37 °C under 10% CO_2. Time-lapse images were taken using an inverted microscope (BZ9000; Keyence, Osaka, Japan) with a 20× Plan Apo Fluor objective lens (Nikon, Tokyo, Japan).

Quantification of muscle cell hypertrophy and lamellipodium formation

Cell quantification was done as described [5]. The distribution of myogenic cell sizes was determined by calculating the percentage

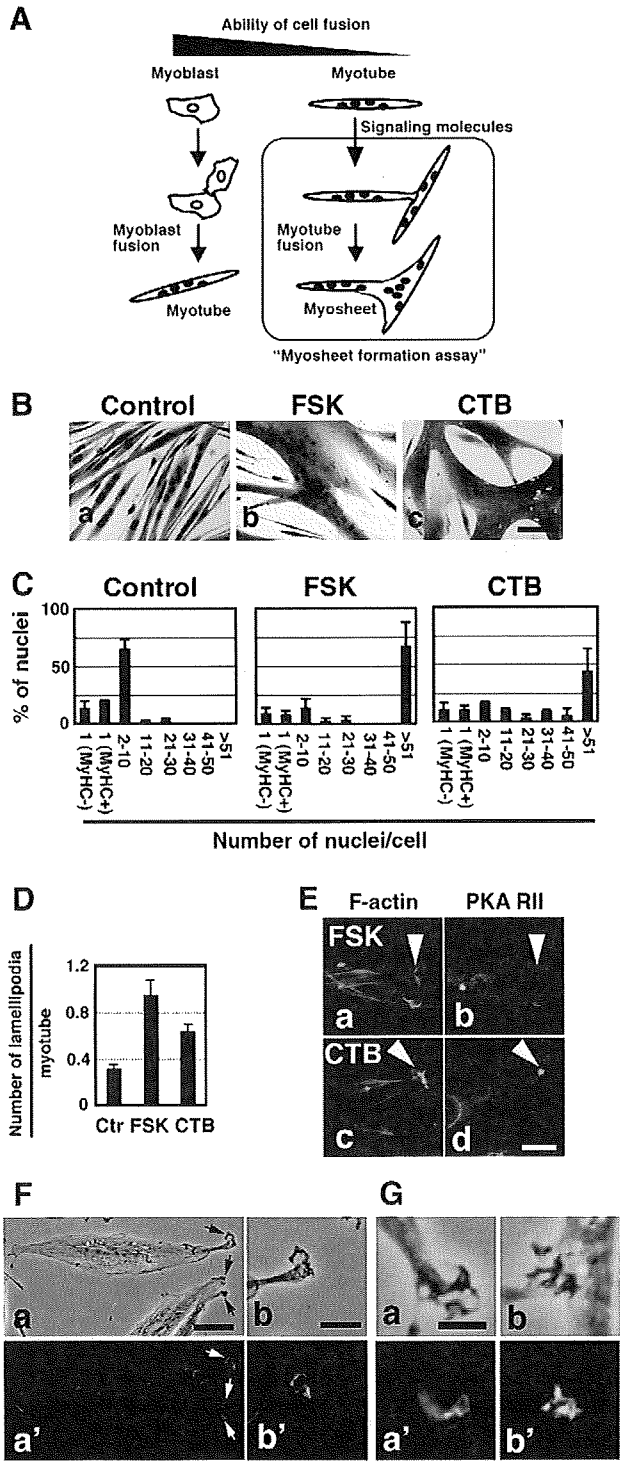

Fig. 1 – CTB induces muscle cell hypertrophy. (A) Myosheet formation assay. The ability of extracellular signaling molecules to enhance myotube fusion can be determined in myotube culture in vitro. (B) Ric10 cells (2×10^4 cells per 35-mm dish) were cultured for 36 h in pmDM (a) or in pmDM supplemented with 24 μM forskolin (b) or 125 ng/ml CTB (c). Then the cells were immunostained for MyHC. Nuclei were counterstained with Mayer's hematoxylin. Images were obtained by bright field microscopy. Scale bar: 40 μm. (C) Histograms represent the distribution of myogenic cells with different numbers of nuclei in unstimulated (left panel), forskolin-stimulated (middle panel), or CTB-stimulated (right panel) cultures after 36 h of differentiation culture. Mononucleated cells were classified to two subpopulations: one expressed MyHC (MyHC+) and the other did not (MyHC−). (D) Ric10 cells (1×10^4 cell per 35-mm dish) were cultured for 48 h in pmDM (Ctr), pmDM supplemented with 24 μM forskolin (FSK), or pmDM supplemented with CTB. Actin filaments in lamellipodia were stained with Alexa Fluor 546-labelled phalloidin. The number of lamellipodia in at least 100 myotubes per dish was counted under a phase-contrast and epifluorescence microscope. Each myotube formed 0, 1, or 2 lamellipodia at their polar ends. Averages and standard deviations of numbers of lamellipodia per myotube from three independent cultures are shown. (E) After 36 h of culture in pmDM containing forskolin (a and b) or CTB (c and d), Ric10 cells were subjected to immunostaining with anti-PKA RII antibody (RII) (b and d). Actin filaments were stained with Alexa Fluor 546-labelled phalloidin (a and c). Arrowheads represent the leading edges of lamellipodia. Images were obtained by epifluorescence microscopy. Scale bars: 20 μm. (F, G) After 36 h of culture in pmDM containing forskolin, small myotubes of Ric10 cells were subjected to staining with Alexa Fluor 488-labelled CTB (a' and b' in F), or fPEG-Chol (a' and b' in G). Arrows represent the leading edges of lamellipodia. Images were obtained by bright field (upper panels in F and G) and epifluorescence (lower panels in F and G) microscopy. Scale bars: 50 μm in (Fa), 10 μm in the others.

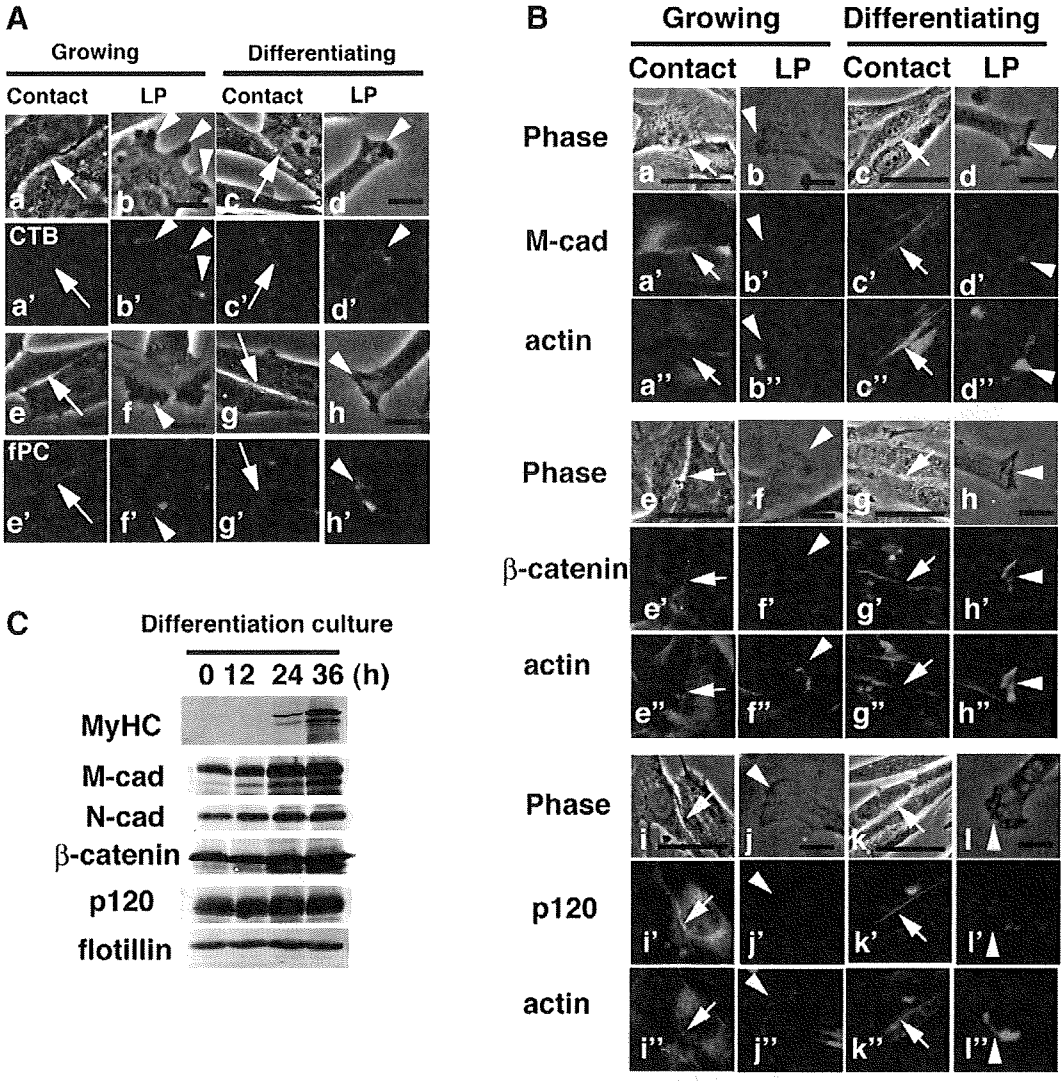

Fig. 2 – Raft markers and adhesion molecules are localized at leading edge of lamellipodia and cell–cell contacts. (A) Ric10 cells (2×10^4 cells per 35-mm dish) were cultured in pmGM for 24 h and then cultured in pmGM (a, b, e, and f) or in pmDM for 30 h (c, d, g, and h). Raft markers GM1 (a'–d') and cholesterol (e'–h') were visualized by Alexa 488-labelled CTB (CTB) and fPEG-Chol (fPC), respectively. GM1 and cholesterol were enriched in cell–cell contact regions (Contact; a, c, e and g) and lamellipodia (LP; b, d, f and h) under both growing and differentiation-inducing conditions. Arrows represent plasma membranes at cell contacts. Arrowheads represent the leading edges of lamellipodia. Images in (a–h) were obtained by phase-contrast microscopy, and those in (a'–h') were obtained by epifluorescence microscopy. Scale bars: 10 μm. (B) Ric10 cells (2×10^4 cells per 35-mm dish) were cultured for 30 h in pmDM. Then the cells were subjected to immunostaining with anti-M-cadherin antibody (a'–d'), anti-β-catenin (e'–h'), or anti-p120-catenin (p120) (i'–l'). Actin filaments were stained with Alexa Fluor 546-labelled phalloidin (a"–l"). Arrows represent plasma membranes at cell contacts. Arrowheads represent the leading edges of lamellipodia. Images in (a–l) were obtained by phase-contrast microscopy, and those in (a'–l' and a"–l") were obtained by epifluorescence microscopy. Scale bars: 10 μm. (C) Total lysates (20 μg of proteins) were prepared from cells that were cultured in pmDM for 0 h (lanes 1), 12 h (lanes 2), 24 h (lanes 3), or 36 h (lanes 4), and then subjected to immunoblot analysis for the represented proteins. Flotillin, a marker of lipid rafts, was used as a loading control.

of nuclei in myogenic cells with different numbers of nuclei in the total number of nuclei (myoblasts plus myotubes).

Fractionation of detergent-resistant membranes

Ric10 cells (1×10^5 cells/100 μl spot) were micromass cultured. A total 1×10^6 cells/10 spots were cultured in two 100-mm dishes for 24 h in pmGM and then further incubated for 12 h in pmDM. The cells were lysed in 0.2 ml of ice-cold lysis buffer (0.5% Trion X-100, 50 mM MES (pH 6.0), 50 mM NaCl, 5 mM $MgCl_2$, and 2.5 mM EGTA) containing protease inhibitor (Complete Protease Inhibitor Cocktail EDTA-free; Roche, Mannheim, Germany) for 30 min on ice. Protein concentrations in aliquots of cell lysates were determined using a BCA kit (Sigma). An aliquot of the lysate containing 319–434 μg protein was mixed with OptiPrep (Axis-Shield, London, UK) and fractionated in a 3 ml Optiprep gradient

according to manufacturer's instructions (Caveolae/Rafts Isolation Kit; Sigma). Ten fractions were collected from the top and 30 μl of each fraction was analyzed by immunoblotting. The PVDF membranes were scanned, and the signal intensity of each band was quantified using Image J software (NIH). The distribution of the protein in each fraction was determined by calculating the ratio of the signal intensity of the protein band in each fraction to the sum of the signal intensity in all fractions. Changes of protein distributions in MCD-treated cells were represented as "% Difference", which was estimated as follows: [distribution of the protein in each fraction of MCD-treated cells (%)] − [distribution of the protein in each fraction of untreated control cells (%)].

Online supplementary materials

Fig. S1 shows the expression levels of MyHC and M-cadherin in myoblasts stimulated with forskolin and CTB. Fig. S2 shows detection of M-cadherin at the leading edge of lamellipodia in differentiating myoblasts without permeabilization. Fig. S3 shows the lipid raft-dependent distributions of N-cadherin and NCAM on the leading edge of lamellipodia in differentiating myoblasts. Fig. S4 shows the distributions of adhesion molecules on the detergent-resistant membrane fractions of differentiating myoblasts. Movies 1 and 2 show the dynamic clustering and dispersion of lipid rafts at the leading edge of lamellipodia of differentiating myoblasts. Movies 3 and 4 show the dynamic clustering and dispersion of lipid rafts at the ruffling membranes of differentiating myoblasts.

Results

Cholera toxin B subunit induces muscle cell hypertrophy

Terminally differentiated multinucleated myotubes tend to lose the capacity to fuse during terminal muscle differentiation. Previously, we showed that cAMP-elevating reagents such as an adenylate cyclase activator forskolin induce cell fusion between myotubes, which give rise to a large sheet-like syncytium designated a "myosheet" [5]. To identify the key surface molecules that render an area of the plasma membrane fusion-competent, we determined the ability of extracellular signaling molecules to enhance myosheet formation in vitro (Fig. 1A). Mouse myogenic progenitor cells C2C12 or Ric10 [1,5] were stimulated with a series of growth factors, ligands, or extracellular matrices. We found that CTB induced myosheet formation in mouse myogenic cells. Ric10 cells were cultured for 36 h in pmDM supplemented with CTB. When plated at low density (2×10^4 cells per 35-mm dish), Ric10 cells gave rise to small bipolar myotubes under differentiation-inducing conditions (Fig. 1Ba). In contrast, Ric10 treated with CTB formed large syncytia that were similar to myosheets formed in forskolin-stimulated Ric10 cells (Fig. 1Bb and c). In control cultures, most myotubes contained 2 to 10 nuclei, and the maximum number of nuclei in myotubes was no more than 30 throughout the culture period (Fig. 1C left panel). In contrast, CTB- or forskolin-stimulated Ric10 cells formed extra-large myotubes containing more than 51 nuclei (Fig. 1C middle and right panels). Both the ratio of the number of nuclei in myotubes to the total number of nuclei, which is called the "fusion index", and the differentiation index, which represents the ratio of the number of nuclei in MyHC-expressing cells to the total number of nuclei, reached similar levels after 36 h of culture in unstimulated and forskolin- or CTB-stimulated Ric10 cells (Fig. 1C). In addition, expression levels of the muscle differentiation marker sarcomeric MyHC and the muscle-specific adhesion molecule M-cadherin were similar in unstimulated and forskolin- or CTB-stimulated Ric10 cells (Supplementary Fig. S1). The results imply that CTB enhances cell fusion between myotubes independently of stimulation of cell differentiation in a manner similar to forskolin.

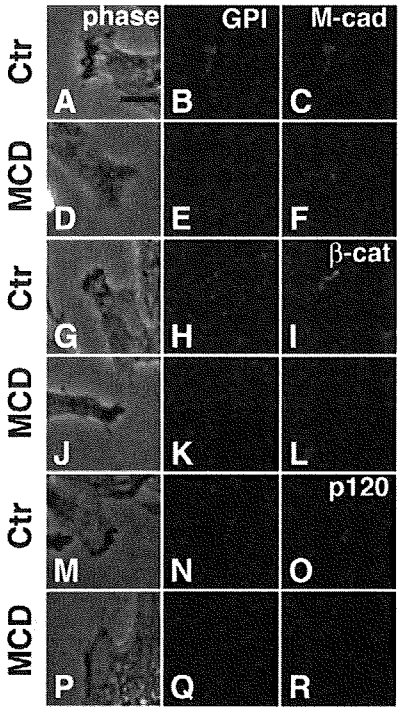

Fig. 3 – Accumulation of adhesion proteins at leading edge of lamellipodia is completely dependent on lipid raft structures. GSS25 cells, a Ric10 cell-derived clone expressing GFP-GPI, (2×10^4 cells per 35-mm dish) were cultured in pmDM for 30 h and then incubated a further 30 min in pmDM (Ctr)(A–C, G–I, and M–O) or in pmDM supplemented with 5 mM MCD (MCD) (D–F, J–L, and P–R). Lipid rafts were visualized by GFP-GPI, which was further probed with anti-GFP antibody (B, E, H, K, N and Q). M-cadherin (C and F), β-catenin (I and L), and p120-catenin (O and R) were detected with specific antibody. Images in the left panels were obtained by phase-contrast microscopy, and those in other panels were obtained by epifluorescence microscopy. Scale bars: 10 μm.

Forskolin enhanced lamellipodium formation in myotubes prior to cell fusion through activation of cyclic adenosine monophosphate-dependent protein kinase (PKA) (Fig. 1D) [5]. To determine the effects of CTB on the formation of lamellipodia in small bipolar myotubes, Ric10 cells were seeded at low density (1×10^4 cells per 35-mm dish) and cultured for 48 h in pmDM supplemented with CTB. CTB treatment significantly increased the frequency of lamellipodium formation in Ric10 myotubes, as shown in forskolin-treated Ric10 cells (Fig. 1D). Immunostaining analysis showed that the type II regulatory subunit of PKA was enriched in the leading edge of lamellipodia where F-actin was

accumulated in CTB-treated Ric10 cells (Fig. 1Ec and d), as shown in forskolin-treated Ric10 cells (Fig. 1Ea and b). Taken together with the results here, CTB is likely to enhance myotube fusion in a manner similar to forskolin.

The lipid raft marker ganglioside GM1 is a major binding target of CTB. Fluorescent dye-conjugated CTB demonstrated the presence of GM1 in the leading edge of lamellipodia of small myotubes that were stimulated with forskolin (Fig. 1F). Marked accumulation of fPEG-Chol in the leading edge of lamellipodia of forskolin-stimulated myotubes also suggests the clustering of lipid rafts (Fig. 1G) because cholesterol is well known to be enriched in lipid rafts. The results suggest that lipid rafts are involved in the capacity of lamellipodia for plasma membrane fusion.

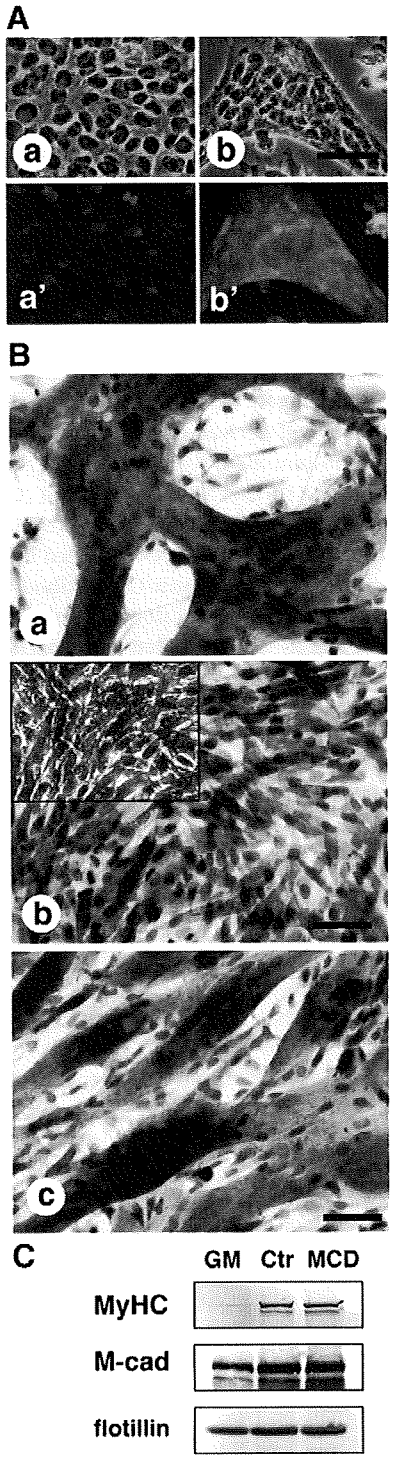

Adhesion molecules accumulate at leading edge of lamellipodia

CTB induces lipid raft aggregation or patching [27]. The CTB-induced myosheet formation implicates the role of lipid rafts in cell fusion of mononucleated myogenic progenitor cells as well as myotubes. If this is indeed the case, lipid rafts may play a role in cell fusion exclusively under myogenic differentiation-inducing conditions because growing myogenic cells don't fuse with each other. Next, a series of experiments were done to elucidate the role of lipid rafts in cell fusion of mononucleated myogenic progenitor cells. First, the distributions of raft markers were determined in growing and differentiating myoblasts. Binding of fluorescent CTB showed that GM1 was accumulated in cell-to-cell contact regions and the leading edge of lamellipodia under both growth- and differentiation-inducing conditions (Fig. 2Aa–d). fPEG-Chol was also enriched in cell-to-cell contact regions and the leading edge of lamellipodia under both culture conditions (Fig. 2Ae–h). The results indicate that the distribution of lipid rafts is not affected by culture conditions.

Second, the distribution of M-cadherin and its associated proteins in sites of the plasma membrane in which lipid rafts clustered was determined by immunostaining analyses. M-cadherin accumulated at cell contacts in both growing and differentiating myoblasts (Fig. 2Ba and c). M-cadherin also accumulated at the leading edge of lamellipodia during differentiating culture exclusively (Fig. 2Bd) but not at the leading edge of lamellipodia in growing culture (Fig. 2Bb). An antibody against the extracellular domain of M-cadherin also recognized M-cadherin at the lamellipodia of differentiating myoblasts, the membrane of which was not

Fig. 4 – MCD prevents plasma membrane union of myogenic cells. (A) Ric10 cells (1×10^5 cells per 35-mm dish) were cultured in pmGM for 30 h and then further cultured in pmGM (a and a') or pmDM (b and b') for up to 24 h. The cells were fixed and subjected to immunostaining for MyHC (red) in (a' and b'). Cell nuclei were stained with DAPI (blue). (a') and (b') show the same areas as (a) and (b), respectively. Images were obtained by phase-contrast (a and b) and epifluorescence (a' and b') microscopy. Scale bar: 50 μm. (B) Ric10 cells (1×10^5 cells per 100 μl of spot) were cultured in micromass in pmGM for 24 h, and then further cultured in pmDM (a) or pmDM supplemented with 5 mM MCD (b) or 5 mM MCD preloaded with cholesterol (c) for up to 16 h. Then the cells were fixed and subjected to immunostaining with anti-MyHC antibody. Nuclei were counterstained with Mayer's hematoxylin. Images were obtained by bright field (a, b and c) and phase-contrast (an inlet in (b)) microscopy. The inlet in (b) shows complete inhibition of cell fusion in MCD-treated culture. Scale bar: 50 μm. (C) Ric10 cells (1×10^5 cells per 100 μl of spot) were cultured in micromass in pmGM for 24 h (lane 1) and then further cultured in pmDM (lane 2) or pmDM supplemented with 5 mM MCD (lane 3) for up to 16 h. Total cell lysates (20 μg) were subjected to immunoblot analysis for the represented proteins. Flotillin, a marker of lipid rafts, was used as a loading control.

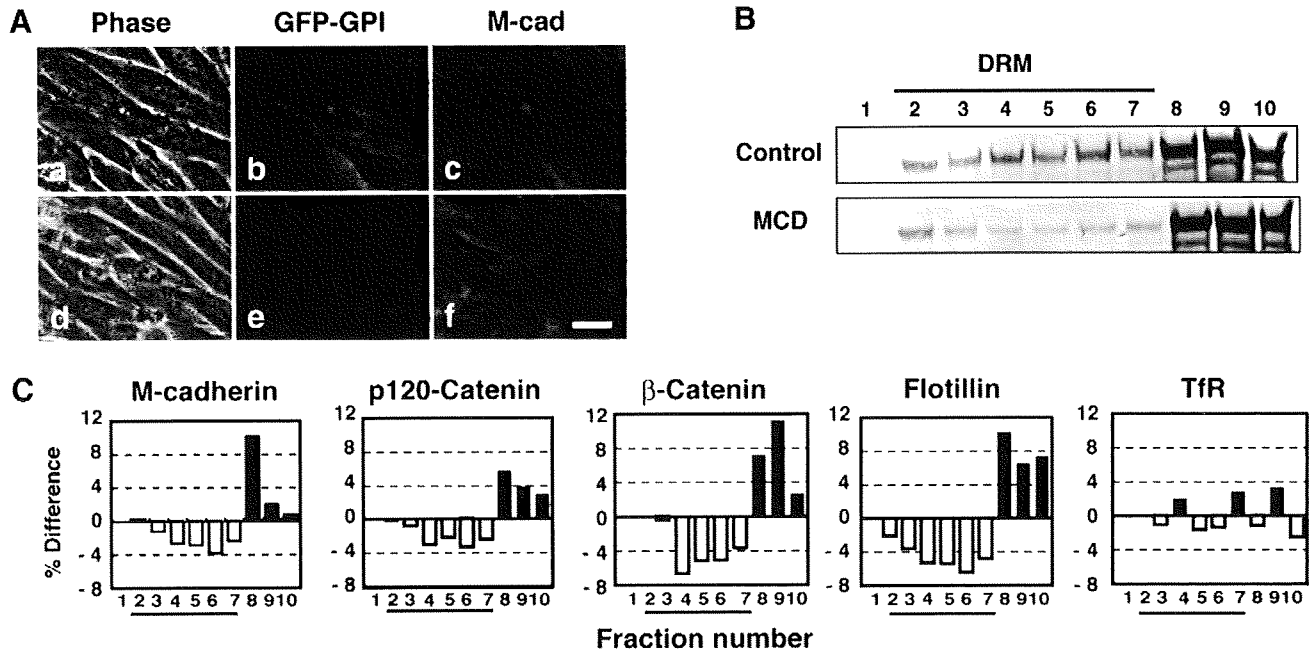

Fig. 5 – MCD impairs accumulation of adhesion proteins at lipid rafts but not adhesion of myogenic cells. (A) GSS25 cells were cultured in micromasses for 12 h in pmDM (Ctr)(a–c) or pmDM supplemented with 5 mM MCD (MCD)(d–f). The cells were subjected to immunostaining with anti-GFP (b and e) and anti-M-cadherin (c and f) antibodies. (a) and (d) show the same areas as (b and c) and (e and f), respectively. Scale bars: 25 μm. (B) The distribution of M-cadherin in each fraction (30 μl) of untreated (Control) or MCD-treated GSS25 cells (MCD) was analyzed by immunoblotting with the appropriate antibody. The line represents the detergent-resistant membrane fractions. (C) The redistribution of the adhesion proteins M-cadherin, p120-catenin, and β-catenin, in each fraction of MCD-treated cells is represented as the % difference of adhesion proteins in each fraction of control cultures. Flotillin was used as a marker of lipid raft. Transferrin receptor (TfR) was used as a marker of non-raft membrane. The lines represent the detergent-resistant membrane fractions. Similar results were obtained from more than two independent experiments. Representative data were shown.

permeabilized (Supplementary Fig. S2), implying that M-cadherin maintains a transmembrane position independent of cell contacts. β-catenin and p120-catenin, which are associated with the intracellular domain of M-cadherin, were localized at the leading edge of lamellipodia of differentiating but not growing myogenic cells, although they continuously accumulated at cell contacts (Fig. 2Be–h and i–l). The protein levels of M-cadherin increased during myogenic terminal differentiation (Fig. 2C), and might contribute to its localization at the leading edge of differentiating cells. The levels of β-catenin, p120-catenin, and N-cadherin also increased slightly during myogenesis. In addition, N-cadherin and NCAM, accumulated at the leading edge of lamellipodia of differentiating myoblasts (A. Mukai and N. Hashimoto, unpublished), although NCAM also accumulated there in growing myoblasts.

Accumulation of adhesion proteins at lamellipodia depends on lipid rafts

Differentiation culture-dependent accumulation of adhesion proteins at the leading edge of lamellipodia suggests that lipid raft structures ferry the adhesion proteins to the site. A species of Ric10 cells constitutively expressing GFP-GPI, designated GGS25, was established to visualize lipid rafts in living cells. A cholesterol-binding agent MCD removes cholesterol from the plasma membrane and disrupts lipid rafts [28]. GSS25 cells were cultured in pmDM for 30 h and then exposed to 5 mM MCD for 30 min. MCD disrupted lipid rafts and impaired the accumulation of M-cadherin, N-cadherin, NCAM, β-catenin, and p120-catenin at the leading edge of lamellipodia, resulting in their homogenous distribution throughout the whole plasma membrane (Fig. 3) (Supplementary Fig. S3). The results suggest that lipid rafts are required for the accumulation of adhesion-related proteins at the presumptively fusion-competent site of the plasma membrane in lamellipodia and play a role in cell adhesion that is prerequisite for membrane fusion.

Lipid rafts are required for plasma membrane fusion of myogenic cells

Myogenic cell fusion consists of a series of steps including cell–cell contact, recognition, adhesion, and plasma membrane breakdown/union. To assess the ability of a membrane to fuse, Ric10 cells were seeded at high cell density (1×10^5 cells per 35-mm dish). The high cell density culture allowed cell–cell contact and adhesion of Ric10 cells within a day of plating. When cultured in growth medium, Ric10 cells adhered to each other but didn't fuse during 24 h of culture after plating (Fig. 4Aa). By contrast, when the medium was switched to pmDM, mononucleated progenitor cells gave rise to multinucleated myotubes within 24 h of differentiation culture (Fig. 4Ab). The results show that cell adhesion is not sufficient for

membrane fusion, and that the plasma membrane union of mononucleated myogenic progenitor cells is highly dependent on the differentiation-inducing condition.

To determine whether lipid rafts are involved in the regulation of the plasma membrane union, Ric10 cells were cultured in micromass. Under the micromass culture condition, cell–cell contact, recognition, and adhesion were completed soon after seeding. When the medium was switched to pmDM, myoblasts gave rise to myotubes within 16 h of culture (Fig. 4Ba). In contrast, MCD-treated cells did not form multinucleated myotubes (Fig. 4Bb). In addition, the inhibition of myotube formation by MCD was rescued by prior loading of MCD with cholesterol [19,29] (Fig. 4Bc). However, in spite of the suppression of membrane fusion, MCD did not impair the expression of the myogenic differentiation marker MyHC and the muscle-specific adhesion molecule M-cadherin (Fig. 4C).

To determine the distributions of lipid rafts and M-cadherin, GGS25 cells were cultured in micromass and then treated with MCD. In control cultures, GFP-GPI and M-cadherin colocalized at the cell–cell contact regions (Fig. 5Aa–c). MCD severely disrupted lipid rafts (Fig. 5Ae). However, in contrast to the leading edge of lamellipodia, M-cadherin remained at cell contact points where lipid raft structures had broken down (Fig. 5Ad–f). In addition, MCD didn't affect the expression levels of M-cadherin (Fig. 4C). The results indicate that once cell adhesion is established in micromass culture, it can be maintained even when lipid rafts were disrupted, although lipid rafts are assumed to be required for establishing cell adhesion. Cellular fractionation experiments show that MCD disrupted lipid raft structures and that M-cadherin, β-catenin and p120-catenin were translocated from the lipid rafts to soluble fractions (Fig. 5B and C) (Supplementary Fig. S4) even though a part of lipid rafts still remained in micromass culture treated with MCD (see flotillin in Supplementary Fig. S4). However, cell adhesion did not seem to be impaired by MCD (Fig. 5Ad). Therefore, it is assumed that MCD prevents myogenic cell fusion through suppression of membrane union in micromass culture, but does not prevent the preceding steps, such as cell adhesion.

Lateral dispersion of lipid rafts from presumptive fusion sites

The present results suggest that cholesterol-enriched lipid rafts cluster at the presumptive fusion site and are required for cell adhesion and membrane fusion. However, membrane fusion takes place within the cholesterol-free areas of the myogenic cell plasma membrane [11]. The cholesterol concentration of the membrane decreases prior to membrane union because an increase in membrane fluidity is required for union. To understand this discrepancy, clustering and dispersion of lipid rafts at the leading edge of lamellipodia were observed in GSS25 cells using GFP-GPI as a raft marker. Our preliminary experiments showed that lipid rafts at the leading edge repeated the clustering-dispersion cycles quickly (Supplementary Movies 1 and 2). Therefore, the redistribution of lipid rafts during the initial contact and membrane union was visualized using GFP-GPI and sequentially observed every 60 s by time-lapse recording. Lipid raft structures remained constant at points of cell contact, and membrane fusion was not induced there even under the differentiation-inducing condition (Fig. 6A). In contrast, the leading edge of the lamellipodium fused to the opposing plasma membrane within a couple of hours after initial contact under the differentiation-inducing condition (Fig. 6B). The lamellipodium moved quickly, and lipid rafts repeatedly clustered and diffused, even after the initial contact with a fusion partner. One hour later, the lamellipodium stopped moving and lipid rafts clustered at the leading edge, which adhered to an adjacent cell (Fig. 6Bb and c). Then, prior to membrane fusion, lipid rafts were laterally dispersed from the center of the lamellipodium (Fig. 6Bd). Soon after, the lipid raft-free area of the plasma membrane started to fuse with the opposing membrane (Fig. 6Be). The results suggest that the dynamic clustering/dispersion of lipid rafts at the leading edge of lamellipodia is essential for plasma membrane fusion of myogenic

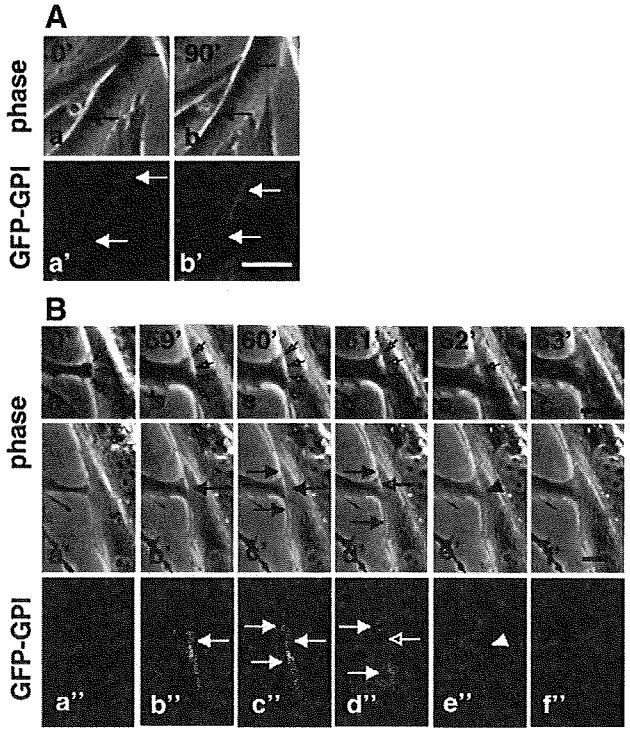

Fig. 6 – Dynamic clustering and dispersion of lipid rafts at leading edge of lamellipodia prior to membrane fusion. (A) GSS25 cells (2×10^4 cells per 35-mm dish) were cultured for 36 h in pmDM. Changes in distribution of lipid rafts were recorded by phase-contrast, epifluorescent, time-lapse microscopy. Images were obtained at the indicated time points. Arrows indicate the robust distribution of lipid raft marker GFP-GPI at cell contacts. Scale bar: 10 μm. (B) The process of cell fusion between in GSS25 culture was recorded by phase-contrast, epifluorescent, time-lapse microscopy. The lamellipodia of one myogenic cell fused to the lateral plasma membrane of another myogenic cell. Images were obtained at the indicated time points. Open arrows in (a–e) represent the cell contact site where the opposed membranes did not fuse each other yet. Arrowheads in (e, e' and e") indicate the initiation site of membrane fusion. Filled arrows in (b'–d' and b"–d") represent the areas where lipid rafts clustered. Open arrows in (d, d' and d") represent the presumptively fusion-competent site that lacks lipid rafts. Cell-to-cell contact areas in (a'–f') were enlarged in the upper panels. Scale bars: 5 μm.

cells. Similar cycling behavior of lipid rafts was also found in the ruffling membranes of myoblasts and myotubes (Supplementary Movies 3 and 4).

Lipid raft-dependent redistribution of adhesion proteins at presumptive fusion sites

Adhesion proteins were accumulated at the presumptive fusion sites in a lipid raft-dependent fashion (Fig. 3). Thus, the redistribution of adhesion complexes at the presumptive fusion sites was determined in GSS25 cells. M-cadherin, p120-catenin and β-catenin were colocalized with lipid rafts at the leading edge of lamellipodia, which adhered to an adjacent cell (Fig. 7A–D, I–L and Q–T). Then, they were removed from the center of the lamellipodium prior to membrane fusion when lipid rafts were laterally dispersed (Fig. 7E–H, M–P and U–X). The results suggest that adhesion complexes are removed from the presumptive fusion sites just prior to membrane fusion depending on the lateral dispersion of lipid rafts. The redistribution of adhesion complexes may be required for plasma membrane fusion.

Role of dynamic redistribution of lipid raft in myogenic cell fusion

Taken together with the results reported here, the process of myogenic cell fusion can be summarized as shown in Fig. 8. The clustering of lipid rafts provides a platform to which adhesion molecules are tethered, rendering the leading edge adhesion-competent (Fig. 8A, B and C). Dispersion of lipid rafts after establishing cell adhesion gives rise to cholesterol- and adhesion complex-free, fusion-competent sites of the plasma membrane (Fig. 8D, E and F). The repeated clustering/dispersion of lipid

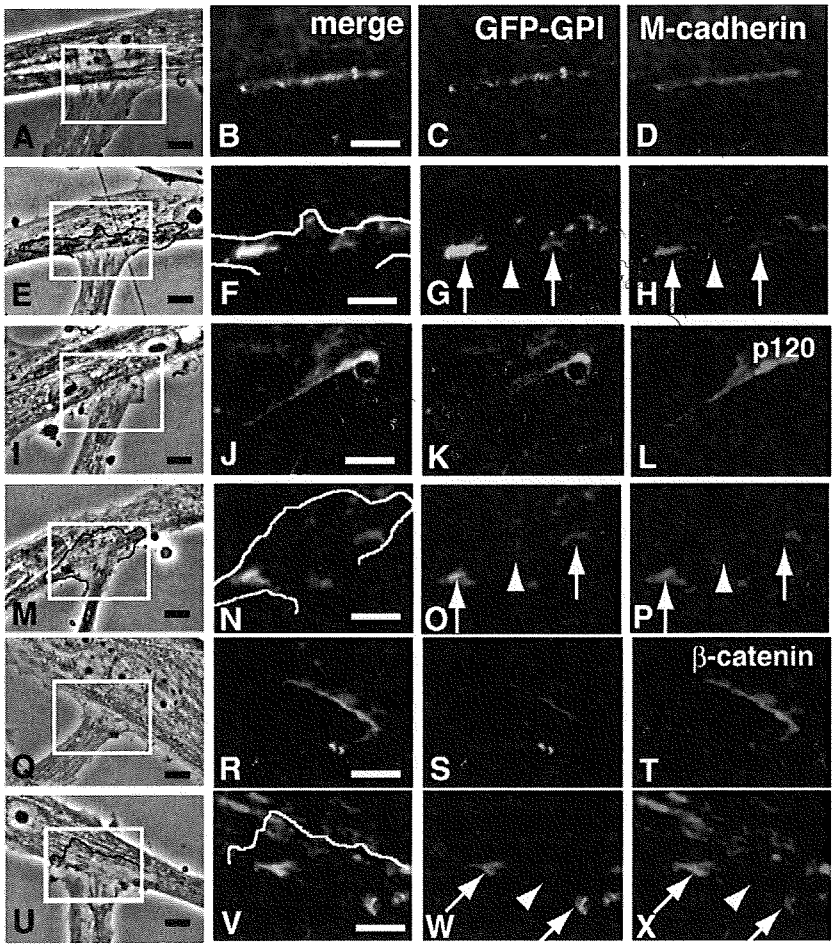

Fig. 7 – Redistribution of M-cadherin accompanies dynamic dispersion of lipid rafts at the leading edge of lamellipodium prior to membrane fusion. GGS25cells (2×10^4 cells per 35-mm dish) were cultured in pmDM for 30 h. Lipid rafts were visualized by GFP-GPI, which was further probed with an anti-GFP antibody (C, G, K, O, S and W). M-cadherin (D and H), p120-catenin (L and P) and β-catenin (T and X) were detected with specific antibodies. Images in (C and D), (G and H), (K and L), (O and P), (S and T) and (W and X) were merged in (B), (F), (J), (N), (R) and (V) respectively. Squares in (A), (E), (I), (M), (Q) and (U) are enlarged areas in (B–D), (F–H), (J–L), (N–P), (R–T) and (V–X) respectively. Images in (A, E, I, M, Q and U) were obtained by phase-contrast microscopy, and those in other panels were obtained by epifluorescence microscopy. Line drawings in (E, F, M, N, U and V) represent the edge of the lamellipodium. Arrows represent the lipid rafts where M-cadherin, p120-catenin or β-catenin clustered. The arrow heads represent the presumptively fusion-competent site that lacks lipid rafts, M-cadherin, p120-catenin or β-catenin. In (E–H), (M–P) and (U–X), the lamellipodia went over the other cells. Scale bars: 10 μm.

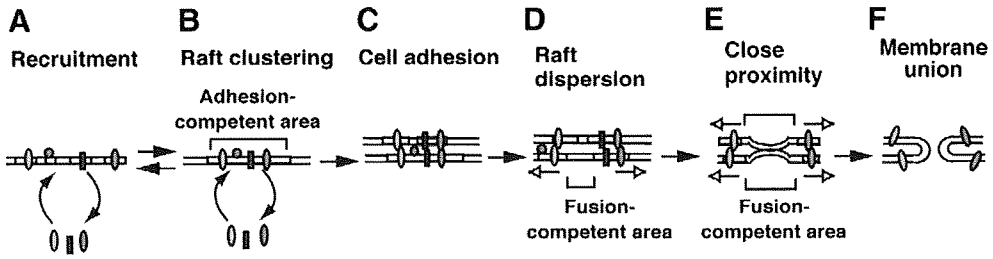

Fig. 8 – Essential role of dynamic clustering and dispersion of lipid rafts in establishing fusion competence of myogenic cells. (A and B) Lipid rafts repeat the cycle of clustering and dispersion in the leading edge of lamellipodia. The putative recruitment cycle of adhesion molecules between cytoplasm and lipid rafts is possible but has not been demonstrated. Clustering of lipid rafts induces the accumulation of adhesion molecules at the leading edge of lamellipodia and renders the area adhesion-competent (B). (C) The leading edge contacts and adheres to an adjacent cell. (D) Lateral dispersion of lipid rafts (represented by open arrows) gives rise to cholesterol- and adhesion molecule-free sites and renders the leading edge of lamellipodia fusion-competent. (E) Lateral dispersion of lipid rafts at the leading edge induces dispersion of lipid rafts on the opposing membrane (represented by open arrows). Then the opposed lipid bilayers are brought into close proximity. (F) The opposed membranes unite, and the fused area of the membranes spreads.

rafts at the leading edge of lamellipodia is essential for establishing fusion-competent sites in the plasma membrane of myogenic cells.

Discussion

We demonstrated that the dynamic clustering and dispersion of lipid rafts are required for the regulation of cell adhesion and membrane union during myogenic cell fusion. The leading edge of a lamellipodium is a presumptively fusion-competent site of the plasma membrane of myogenic cells [5]. A set of adhesion molecules accumulates at the leading edge of lamellipodia of differentiating myogenic cells in a lipid raft-dependent fashion. Lipid rafts at the leading edge of lamellipodia probably play the role of a platform tethering the adhesion molecules. The present results suggest that tethering adhesion molecules to the lipid raft in the leading edge of lamellipodia allows the molecules to function synergistically in the recognition/cell adhesion steps under a strict spatiotemporal control.

Plasma membrane breakdown/union is a final step of myogenic cell fusion. Mechanisms controlling plasma membrane breakdown/union have been studied biochemically and ultrastructurally by utilizing freeze-fracture techniques [11,12,30]. The concentration of membrane cholesterol decreases in differentiating myoblasts, producing a marked augmentation of membrane fluidity [31]. Membrane fusion takes place at discrete spots of the plasma membrane that are cholesterol-free. The decrease of membrane cholesterol is prerequisite for membrane breakdown/union because cholesterol is involved in the maintenance of plasma membrane fluidity. Therefore, dynamic redistribution of membrane cholesterol has been proposed to be a key event in plasma membrane fusion of myogenic cells.

Fusion of lipid bilayers in an aqueous environment comprises two conditions: close proximity of the membranes and destabilization of the boundary between the hydrophilic and hydrophobic portions of the bilayer [32]. We showed that dynamic lateral dispersion of lipid rafts at the leading edge of lamellipodia provided fusion-competent, cholesterol-free or low sites of the plasma membrane. Time-lapse observation reveals that the lipid raft-free sites fused to the opposing membrane of an adjacent cell. The results suggest that lateral dispersion of lipid rafts results in the reduction of membrane cholesterol at the presumptive fusion site followed by the increase of membrane fluidity and destabilization of the lipid bilayers [33].

The complex of adhesion molecules physically impairs close proximity of the opposed plasma membranes although they are relevant for cell adhesion. Lateral dispersion of lipid rafts also resulted in redistribution of adhesion complexes containing M-cadherin, β-catenin and p120-catenin that are tethered to lipid rafts. Consequently, lateral dispersion of lipid rafts at the presumptive fusion site provides adhesion complex-free spots of membrane that can be brought into close proximity. Therefore, the dynamic redistribution of lipid rafts at the presumptive fusion site is critical to render the discrete site of plasma membrane fusion-competent.

Cell adhesion and membrane fusion are sequential steps in myogenic cell fusion. However, either step requires distinct microcircumstances in the plasma membrane. To establish cell adhesion, the plasma membrane at the presumptive fusion site must contain enough cholesterol to maintain rigid lipid bilayers that hold adhesion complexes. In contrast, membrane cholesterol decreases in the same site prior to membrane fusion. In addition, adhesion complexes must be removed from the fusion site although they are relevant for cell adhesion. The mechanisms that control the rapid redistribution of membrane cholesterol and adhesion proteins during cell adhesion and membrane fusion steps have been unknown. Our data suggest that the clustering of lipid rafts provides a robust platform to tether adhesion molecules to the presumptive fusion site prior to cell contact, and that subsequent lateral dispersion of lipid rafts removes the adhesion molecules from the presumptive fusion site prior to membrane union. Furthermore, the real-time recording indicates that the opposite conditions were established in the plasma membrane of presumptive fusion sites within a couple of minutes by quick redistribution of lipid rafts. Thus, the dynamic clustering and dispersion of lipid rafts enables robust and rapid changes in plasma membrane components at the presumptive fusion site.

Lipid rafts at the leading edge of lamellipodia repeatedly clustered and diffused in the few minutes prior to cell contact, whereas those at the established cell contacts continue to be

accumulated. This dynamic behavior of lipid rafts at the leading edge is a prerequisite for their lateral dispersion prior to membrane fusion. Similar dynamic behavior of lipid rafts was also found in the ruffling membrane of myogenic cells. We observed fusion of the ruffling membrane to the opposing membrane (A. Mukai, unpublished). Therefore, we propose here that the dynamic clustering and dispersion of lipid rafts is a common feature of presumptively fusion-competent sites in the plasma membrane of myogenic cells.

Cadherins at the leading edge of lamellipodia of myogenic cells did not have partner molecules to bind to and their localization was completely independent of cell–cell contact. Detection of M-cadherin at the lamellipodia of non-permeabilized myoblasts by an antibody against its extracellular domain strongly suggests that M-cadherin normally maintains a transmembrane position independent of homophilic binding or cell contacts. The colocalization of M-cadherin, β-catenin, and p120-catenin implies that they build up an adhesion complex at the lamellipodia. The present results suggest that cadherins at the leading edge of lamellipodia are maintained as transmembrane proteins and participate in functional adhesion complexes in a cell contact-independent manner.

Membrane fusion does not take place in all areas of the closely abutted plasma membranes of myogenic cells [6] (the present study). Cell-to-cell contact induces micron-size clustering of lipid rafts and accumulation of cadherins in the plasma membrane of cell contact regions. However, membrane fusion was not induced there even under the differentiation-inducing condition. In contrast to the repeated clustering-dispersion of lipid rafts in the leading edge of lamellipodia, the cell contact-induced clustering of lipid rafts continued at cell–cell contact points after cell adhesion was established. High levels of cholesterol in the plasma membrane of cell–cell contact regions might cause rigidity, making the area of plasma membrane incapable of fusion. In addition, stable adhesion complexes might impair close proximity of the opposed plasma membranes.

Taken together with previous works, the coordination and/or balance of multiple signaling pathways is required for the regulation of the sequential steps of myogenic cell fusion. Our data indicate that the dynamic clustering and dispersion of lipid rafts plays a pivotal role in the spatiotemporal coordination of multiple adhesion molecules and catastrophic changes of plasma membrane composition that occur prior to membrane union, demonstrating that lipid rafts control myogenic cell fusion in a hitherto unappreciated mode. Further work determining the molecular pathway, which governs the clustering and dispersion of lipid rafts, will provide a novel conception of the regulation of myogenic cell fusion.

Acknowledgments

This work was supported by grants to N.H. from the Ministry of Health, Labor, and Welfare of Japan.

Appendix A. Supplementary data

Supplementary data associated with this article can be found, in the online version, at doi:10.1016/j.yexcr.2009.07.010.

REFERENCES

[1] M.R. Wada, M. Inagawa-Ogashiwa, S. Shimizu, S. Yasumoto, N. Hashimoto, Generation of different fates from multipotent muscle stem cells, Development 129 (2002) 2987–2995.
[2] M.J. Wakelam, The fusion of myoblasts, Biochem. J. 228 (1985) 1–12.
[3] K.A. Knudsen, L. Smith, S. McElwee, Involvement of cell surface phosphatidylinositol-anchored glycoproteins in cell–cell adhesion of chick embryo myoblasts, J. Cell Biol. 109 (1989) 1779–1786.
[4] E.H. Chen, E.N. Olson, Towards a molecular pathway for myoblast fusion in Drosophila, Trends Cell Biol. 14 (2004) 452–460.
[5] A. Mukai, N. Hashimoto, Localized cyclic AMP-dependent protein kinase activity is required for myogenic cell fusion, Exp. Cell Res. 314 (2008) 387–397.
[6] G. Fumagalli, A. Brigonzi, T. Tachikawa, F. Clementi, Rat myoblast fusion: morphological study of membrane apposition, fusion, and fission during controlled myogenesis in vitro, J. Ultrastruct. Res. 75 (1981) 112–125.
[7] I. Tachibana, M.E. Hemler, Role of transmembrane 4 superfamily (TM4SF) proteins CD9 and CD81 in muscle cell fusion and myotube maintenance, J. Cell Biol. 146 (1999) 893–904.
[8] R.S. Krauss, F. Cole, U. Gaio, G. Takaesu, W. Zhang, J.S. Kang, Close encounters: regulation of vertebrate skeletal myogenesis by cell–cell contact, J. Cell Sci. 118 (2005) 2355–2362.
[9] V. Horsley, G.K. Pavlath, Forming a multinucleated cell: molecules that regulate myoblast fusion, Cells Tissues Organs 176 (2004) 67–78.
[10] J. Prives, M. Shinitzky, Increased membrane fluidity precedes fusion of muscle cells, Nature 268 (1977) 761–763.
[11] T. Sekiya, T. Takenawa, Y. Nozawa, Reorganization of membrane cholesterol during membrane fusion in myogenesis in vitro: a study using the filipin–cholesterol complex, Cell Struct. Funct. 9 (1984) 143–155.
[12] M. Nakanishi, E. Hirayama, J. Kim, Characterisation of myogenic cell membrane: II. Dynamic changes in membrane lipids during the differentiation of mouse C2 myoblast cells, Cell Biol. Int. 25 (2001) 971–979.
[13] R.B. Cornell, S.M. Nissley, A.F. Horwitz, Cholesterol availability modulates myoblast fusion, J. Cell Biol. 86 (1980) 820–824.
[14] N. Hashimoto, T. Murase, S. Kondo, A. Okuda, M. Inagawa-Ogashiwa, Muscle reconstitution by muscle satellite cell descendants with stem cell-like properties, Development 131 (2004) 5481–5490.
[15] N. Hashimoto, T. Kiyono, M.R. Wada, R. Umeda, Y. Goto, I. Nonaka, S. Shimizu, S. Yasumoto, M. Inagawa-Ogashiwa, Osteogenic properties of human myogenic progenitor cells, Mech. Dev. 125 (2008) 257–269.
[16] N. Hashimoto, T. Kiyono, M.R. Wada, S. Shimizu, S. Yasumoto, M. Inagawa, Immortalization of human myogenic progenitor cell clone retaining multipotentiality, Biochem. Biophys. Res. Commun. 348 (2006) 1383–1388.
[17] N. Hashimoto, M. Ogashiwa, Isolation of a differentiation-defective myoblastic cell line, INC-2, expressing muscle LIM protein under differentiation-inducing conditions, Dev. Growth Differ. 39 (1997) 363–372.
[18] N. Hashimoto, M. Ogashiwa, S. Iwashita, Role of tyrosine kinase in the regulation of myogenin expression, Eur. J. Biochem. 227 (1995) 379–387.
[19] A.E. Christian, M.P. Haynes, M.C. Phillips, G.H. Rothblat, Use of cyclodextrins for manipulating cellular cholesterol content, J. Lipid Res. 38 (1997) 2264–2272.
[20] G. Kondoh, Development of glycosylphosphatidylinositol-anchored enhanced green fluorescent protein. One-step visualization of GPI fate in global tissues and ubiquitous cell surface marking, Methods Mol. Biol. (Clifton, N.J 183 (2002) 215–224.